

# The VLA/ALMA Nascent Disk and Multiplicity (VANDAM) Survey of Perseus Protostars. VI. Characterizing the Formation Mechanism for Close Multiple Systems

JOHN J. TOBIN,<sup>1,2,3</sup> LESLIE W. LOONEY,<sup>4</sup> ZHI-YUN LI,<sup>5</sup> SARAH I. SADAVOY,<sup>6</sup>  
MICHAEL M. DUNHAM,<sup>7,6</sup> DOMINIQUE SEGURA-COX,<sup>4</sup> KAITLIN KRATTER,<sup>8</sup> CLAIRE J. CHANDLER,<sup>9</sup>  
CARL MELIS,<sup>10</sup> ROBERT J. HARRIS,<sup>4</sup> AND LAURA PEREZ<sup>11</sup>

<sup>1</sup>Current address: National Radio Astronomy Observatory, 520 Edgemont Rd., Charlottesville, VA 22903, USA

<sup>2</sup>Homer L. Dodge Department of Physics and Astronomy, University of Oklahoma, 440 W. Brooks Street, Norman, OK 73019, USA

<sup>3</sup>Leiden Observatory, Leiden University, P.O. Box 9513, 2300-RA Leiden, The Netherlands

<sup>4</sup>Department of Astronomy, University of Illinois, Urbana, IL 61801

<sup>5</sup>Department of Astronomy, University of Virginia, Charlottesville, VA 22903

<sup>6</sup>Harvard-Smithsonian Center for Astrophysics, 60 Garden St, MS 78, Cambridge, MA 02138

<sup>7</sup>Department of Physics, State University of New York Fredonia, Fredonia, New York 14063, USA

<sup>8</sup>University of Arizona, Steward Observatory, Tucson, AZ 85721

<sup>9</sup>National Radio Astronomy Observatory, P.O. Box O, Socorro, NM 87801

<sup>10</sup>Center for Astrophysics and Space Sciences, University of California, San Diego, CA 92093

<sup>11</sup>Departamento de Astronomía, Universidad de Chile, Camino El Observatorio 1515, Las Condes, Santiago, Chile

## ABSTRACT

We present Atacama Large Millimeter/submillimeter Array (ALMA) observations of multiple protostar systems in the Perseus molecular cloud previously detected by the Karl G. Jansky Very Large Array (VLA). We observed 17 close (<600 AU separation) multiple systems at 1.3 mm in continuum and five molecular lines (i.e., <sup>12</sup>CO, C<sup>18</sup>O, <sup>13</sup>CO, H<sub>2</sub>CO, SO) to characterize the circum-multiple environments in which these systems are forming. We detect at least one component in the continuum for the 17 multiple systems. In three systems, one companion is not detected, and for two systems the companions are unresolved at our observed resolution. We also detect circum-multiple dust emission toward 8 out of 9 Class 0 multiples. Circum-multiple dust emission is not detected toward any of the 8 Class I multiples. Twelve systems are detected in the dense gas tracers toward their disks/inner envelopes. For these 12 systems, we use the dense gas observations to characterize their formation mechanism. The velocity gradients in the circum-multiple gas are clearly orthogonal to the outflow directions in 8 out of the 12 systems, consistent with disk fragmentation. Moreover, only two systems with separations <200 AU are *inconsistent* with disk fragmentation, in addition to the two widest systems (>500 AU). Our results suggest that disk fragmentation via gravitational instability is an important formation mechanism for close multiple systems, but further statistics are needed to better determine the relative fraction formed via this method.

## 1. INTRODUCTION

Star formation typically occurs within dense clouds of molecular gas in the interstellar medium. These clouds of dense gas collapse to form stars when their self-gravity dominates over other sources of support (e.g., thermal pressure, magnetic fields, turbulence, [McKee & Ostriker 2007](#)), forming either a single or multiple star system. Nearly half of Sun-like stars (in terms of stellar mass) are found in binary or higher-order multiple systems ([Duquennoy & Mayor 1991](#); [Raghavan et al. 2010](#)) with typical separations of  $\sim 50$  AU. The frequency of stellar multiplicity strongly depends on stellar mass. Stars more massive than the Sun have a higher fraction of multiplicity, and stars less massive than the Sun have a lower degree of multiplicity; see [Duchêne & Kraus \(2013\)](#) for a recent review. Thus, it is clear that multiple star formation is a common outcome of star formation at all masses, and a comprehensive understanding of the star formation process must also account for multiplicity.

There are two favored routes to explain the formation of multiple star systems: disk fragmentation due to gravitational instability ([Adams et al. 1989](#); [Bonnell & Bate 1994](#); [Stamatellos & Whitworth 2009](#); [Kratte et al. 2010](#)) and turbulent fragmentation of the molecular cloud ([Padoan & Nordlund 2002](#); [Offner et al. 2010](#)). Disk fragmentation will preferentially result in the formation of close ( $< 600$  AU) multiple star systems and requires the existence of a rotationally-supported disk around the primary star. Turbulent fragmentation can result in the formation of both wide and close multiple systems. The initial protostars form with separations  $\sim 1000$  AU (or larger), and depending on their relative motions and masses they can migrate closer together, remain at wide separations, or drift further apart ([Offner et al. 2010](#); [Sadavoy & Stahler 2017](#)). Previously, it was also thought that envelope rotation could play a role in binary/multiple formation (e.g., [Burkert & Bodenheimer 1993](#)), but this is no longer favored given the lack of ordered rotation for most star forming cores ([Tobin et al. 2011](#); [Storm et al. 2014](#); [Fernández-López et al. 2014](#)) and the apparently random orientations of angular momenta (traced by outflow directions) for the wide companion protostars ([Lee et al. 2016](#)). A key prediction of turbulent fragmentation is that the seeds for multiplicity are produced in the pre-stellar phase. Early ALMA survey results suggest tentative agreement with these predictions ([Pineda et al. 2015](#); [Dunham et al. 2016](#); [Kirk et al. 2017](#)), but better statistics are still needed.

Despite the excellent statistics offered by studying field stars, the properties of field star multiples cannot alone reveal the origin of multiplicity. This is because these systems are observed in the present epoch and represent the culmination of Myr to Gyr of dynamical evolution, and to understand the origin of multiplicity, it must be characterized during or shortly after the onset of star formation during the protostellar phase.

Therefore, to gain a more clear picture of multiple star formation, protostars in the earliest phase of the star formation process, known as the Class 0 phase ([André et al. 1993](#)), must be observed. During this phase the forming protostar is enshrouded in a dense, infalling envelope of gas and dust. The high levels of obscuration, however, made searching for multiplicity toward the Class 0 protostars difficult in the infrared, especially at scales less than 1000 AU. Thus, centimeter and millimeter interferometry were necessary to examine the formation of such systems. Early searches detected a number of wide multiple systems ( $> 600$  AU) and a few close ( $< 600$  AU) multiple systems ([Looney et al. 2000](#); [Rodríguez et al. 1998](#); [Brown et al. 2000](#)). Later surveys aimed to improve upon the statistics, and [Chen et al. \(2013\)](#) characterized a number of wide systems in the Class 0 phase, finding that most (67%) Class 0 protostars may begin their lives as part of a wide multiple system. [Maury et al. \(2010\)](#); [Tobin et al. \(2013, 2015a\)](#) aimed to expand the characterization of close multiples, but samples were still too small to provide statistically significant results.

Several efforts were also made to characterize multiplicity in the late protostellar phase (Connelley et al. 2008; Duchêne et al. 2007), the so-called Class I protostars (Dunham et al. 2014). However, even these systems may be too evolved to retain signatures of their formation mechanism given that enough enshrouding material has been accreted/dispersed to enable their detection in the near-infrared.

The VLA/ALMA Nascent Disk and Multiplicity (VANDAM) Survey (Tobin et al. 2015b, 2016b; Segura-Cox et al. 2016) unlocked the distribution of protostellar multiples on scales less than 600 AU (down to  $\sim 20$  AU), thereby sampling the peak of the field solar-type separation distribution. This survey conducted with the NSF’s Karl G. Jansky Very Large Array (VLA) observed all known Class 0 and Class I protostars in the Perseus star forming region, 37 of which are Class 0 protostars (FHSCs and VeLLOs included), 8 are Class 0/I protostars, and 37 are Class I protostars (flat spectrum included) (Tobin et al. 2016b). In addition, 12 Class II sources (pre-main sequence stars with disks) that were bright in the far-infrared were also observed. We adopt a distance of 300 pc as an average distance for the Perseus molecular cloud (Ortiz-León et al. 2018). There may be a distance gradient across the cloud (Ortiz-León et al. 2018; Zucker et al. 2018) with the eastern part of the cloud (IC348) at  $\sim 320$  pc, the central part (NGC 1333) at  $\sim 293$  pc, and the western part (L1448 and L1451) at  $\sim 280$  pc, but 300 pc is adopted for simplicity because these distances are consistent with each other when considering the uncertainties of the current Gaia measurements. We note that these revised distances are in disagreement with the maser parallaxes from Hirota et al. (2008, 2011) which indicated  $\sim 230$  pc. This 230 pc distance was used in Tobin et al. (2016b,a) to determine physical separations and convert continuum flux density to mass. From this sample, 18 systems were identified as multiple with companion separations less than 600 AU, and 16 of these were new detections by the VANDAM survey.

The VANDAM survey greatly increased the detection statistics for protostars on scales less than 600 AU, but the formation mechanism(s) of the multiple systems was difficult to quantify because the VLA survey was continuum-only. Tobin et al. (2016b) argued that the systems with separations beyond  $\sim 500$  AU most likely formed from turbulent fragmentation (Offner et al. 2016); this conclusion was further supported by observations of outflow directions by Lee et al. (2016). For the close multiples detected, disk fragmentation was argued to be the most likely formation mechanism for 17 out of the 18<sup>1</sup> based on their proximity, circumbinary material around some sources, and the double-peaked nature of the separation distribution. Nevertheless, it remains a possibility that the close multiple systems initially formed at wide separations and migrated inward (Offner et al. 2010; Sadavoy & Stahler 2017). However, definitive evidence in favor of disk fragmentation would be finding them embedded within a common, circumbinary/multiple structure that has Keplerian rotation. To search for the presence or lack of such a signature, we observed the sample of 17 (out of 18) close multiple sources in Perseus with the Atacama Large Millimeter/submillimeter Array (ALMA); an additional close multiple system (IRAS 03282+3035/Per-emb-5) was discovered after the program was accepted. ALMA enables simultaneous observation of both dust continuum to look for circum-multiple structure and molecular lines to search for rotation signatures in the surrounding gas (e.g., Takakuwa et al. 2014, 2015; Tobin et al. 2016a).

The results presented here reveal the circum-multiple environment around each close system, such as whether or not there is rotation at small-scales and the presence or absence of surrounding material.

<sup>1</sup> Only one close companion in the VANDAM sample (NGC 1333 IRAS2A/Per-emb-27) had clearly misaligned outflows, indicating that formation within a circumbinary disk is unlikely (Tobin et al. 2015b).

This paper is structured as follows: we discuss the observations and data reduction in Section 2, the results from dust continuum observations and molecular line mapping in Section 3, the implications of the observations in Section 4, and present our conclusions in Section 5.

## 2. OBSERVATIONS AND DATA REDUCTION

The Perseus multiple systems were observed with the ALMA during Cycle 2 on 27 September 2015 with 33 antennas operating and sampling baselines between 32 - 2000 meters. The observations were executed within a 1.8 hour block and the total time spent on each source was  $\sim 2.9$  minutes. The precipitable water vapor was  $\sim 0.7$  mm throughout the observing session. The phase calibrator was J0319+4130 (3C84), the bandpass calibrator was J0237+2848, and the amplitude and absolute flux calibrator was the monitored quasar J0238+166. The absolute flux calibration accuracy is expected to be better than 10%; however, we do not include this uncertainty in our calculations and utilize statistical uncertainties throughout the paper. The correlator was configured to observe a 2 GHz continuum band centered at 232.5 GHz and observed in TDM mode with 128 channels. The three other basebands were allocated to 60 MHz windows with 1960 channels ( $0.083 \text{ km s}^{-1}$  velocity resolution) each and centered on the following molecular transitions:  $^{12}\text{CO}$  ( $J = 2 \rightarrow 1$ ),  $^{13}\text{CO}$  ( $J = 2 \rightarrow 1$ ),  $\text{C}^{18}\text{O}$  ( $J = 2 \rightarrow 1$ ),  $\text{SO}$  ( $J_N = 6_5 \rightarrow 5_4$ ), and  $\text{H}_2\text{CO}$  ( $J = 3_{03} \rightarrow 2_{02}$ ).

The raw visibility data were manually reduced by the North American ARC staff using CASA version 4.5.0, and we additionally performed self-calibration on the continuum data to increase the signal to noise ratio. When possible, we performed 2 rounds of phase self-calibration, first with solution intervals that encompassed the length of an entire on-source scan, then the second round utilized either 12.1 or 6.05 second solution intervals. The shortest possible solution interval was 6.05 seconds, corresponding to the length of a single integration. Following phase self-calibration, we performed amplitude self-calibration using the solution normalization option, which normalizes the amplitude solutions to around the factor 1.0 such that the flux density scaling is not altered. Following the completion of self-calibration on the continuum, the solutions were also applied to the spectral line bands. Self-calibration was possible for 16 out of 17 fields observed, only Per-emb-48 could not be self-calibrated due to insufficient S/N. The resultant noise in the 1.3 mm continuum was  $\sim 0.14 \text{ mJy beam}^{-1}$  and  $\sim 15 \text{ mJy beam}^{-1}$  in  $0.25 \text{ km s}^{-1}$  channels for the spectral line observations. The non-self-calibrated continuum images had a noise level of  $\sim 1 \text{ mJy beam}^{-1}$ .

The data were imaged using the *clean* task within CASA 4.5.0; the ALMA images shown in Figures 1 and 2 for each target were generated using Briggs weighting with a robust parameter of 0.5. Within the *clean* task, we only include data at  $uv$ -distances  $> 50 \text{ k}\lambda$  to mitigate striping in the images from large-scale emission detected on the shortest baseline that could not be properly imaged. The  $^{13}\text{CO}$  ( $J = 2 \rightarrow 1$ ) and  $\text{C}^{18}\text{O}$  ( $J = 2 \rightarrow 1$ ) images were generated with Natural weighting, tapering at  $500 \text{ k}\lambda$ , and also only using the data having  $uv$ -distances  $> 50 \text{ k}\lambda$ . Tapering reduces the weight of longer baseline data in the deconvolution to facilitate the detection of larger, lower surface brightness structures. The typical beam sizes of the continuum and molecular line images are  $0''.27 \times 0''.16$  ( $81 \text{ AU} \times 48 \text{ AU}$ ) and  $0''.35 \times 0''.25$  ( $108 \text{ AU} \times 76 \text{ AU}$ ), respectively.

We note that the phase was very unstable during the course of our observations, and the phase calibrator (J0319+4130) was at  $\sim 10^\circ$  lower elevation than our science targets. As such, there are systematic position offsets in each field up to  $\sim 0''.1$ . Thus, the most precisely measured positions for the observed protostars in Perseus are those listed in Tobin et al. (2016b) from the VLA, despite the higher S/N offered by the ALMA observations.

### 2.1. Data Analysis

With the observed sample of protostellar multiple systems, one of the key observables is the flux density of the resolved sources and that of the surrounding extended structure. We measured the flux densities toward the binary and wide companion systems that fell within the primary beam using Gaussian fitting. First, we fit Gaussians to all compact, individual components that were resolved and/or marginally resolved in the data. The Gaussians were fit using the *imfit* task of CASA 4.7.2. The integrated flux densities and uncertainties, source positions, and Gaussian parameters from *imfit* are given in Table 1. Some sources have clear non-Gaussian, extended components. In these cases, we used *casaviewer* to draw a polygon region encompassing all the extended emission from the sources (out to  $\sim 2''$ , where we still recover all flux) and measure the flux density within the polygon; this value is given as Extended Flux in Table 1. For binary systems, there were many cases where the extended flux was greater than the combined flux densities of the Gaussian fits to the compact sources. This indicates that there is a significant amount of emission in extended, non-Gaussian components.

For the observed molecular lines, we made moment maps over the selected channel ranges where there is spectral line emission. These images are used to assess whether or not there is rotation around a particular multiple system and if there is an outflow.

## 3. RESULTS

### 3.1. Dust Continuum Imaging

We detect a wide variety of structures toward the sample of 17 multiple protostar systems observed by ALMA. The dust continuum images of the Class 0 systems are shown in Figure 1 and the Class I systems in Figure 2. The ALMA observations had high enough angular resolution to resolve the companions in 15 out of the 17 systems. The systems with unresolved companions are Per-emb-2 and Per-emb-18, which have separations of  $0''.08$  ( $\sim 24$  AU). For the 15 systems with resolvable companions, we detected all known components in 12. The companions were not clearly detected for Per-emb-40, Per-emb-55, and Per-emb-48. However, toward Per-emb-55, there is emission at the expected companion position at the  $2\sigma$  level, and for Per-emb-40 there is extended emission toward the companion position that might reflect emission from the companion. Per-emb-48 was among the faintest sources detected by ALMA and self-calibration was not possible for this field. The increased noise from phase decorrelation may have prevented the companion from being detected, but we cannot rule-out that its flux density is below our detection limit.

The Class 0 systems all have some extended emission surrounding the companions. This is demonstrated quantitatively in Table 1, where the total extended flux density (the sum of compact and extended emission) is greater than the flux density from the compact sources. Per-emb-2, Per-emb-18, Per-emb-17, L1448 IRS3B, SVS13A, L1448 IRS3C, and L1448 IRS2 all have clear emission surrounding and/or bridging the companion sources. The degree to which the total flux density is greater varies, sometimes the difference is as small as a few percent (e.g., Per-emb-17), but it can be greater than a factor of two (e.g., Per-emb-33). This emission could be described as a circumbinary disk and/or envelope.

The extended structure surrounding the companions is quite prominent in L1448 IRS3B, SVS13A, Per-emb-18, and Per-emb-2. The extended emission can be described as either spirals or streamers toward L1448 IRS3B, SVS13A, and Per-emb-2 (Figure 1). The spirals in L1448 IRS3B were previously reported in Tobin et al. (2016a). Finally, the extended structures surrounding Per-emb-2 and Per-

emb-18 show evidence of being optically thick at 1.3 mm as evidenced by their emission peaks not being located toward what are assumed protostar positions, but off source, and having smooth surface brightness profiles across their central regions. In all these sources, the VLA imaging in Tobin et al. (2016b) detects the peak emission toward what are assumed to be the positions of the individual protostars, and the ALMA imaging with higher surface brightness sensitivity is able to detect much more extended dust emission than detected by the VLA. Furthermore, the brightest feature in Per-emb-18 is offset to the east; this was a weakly detected feature at 9 mm with the VLA (Tobin et al. 2016b).

Finally, there is less-prominent extended emission toward NGC1333 IRAS2A and L1448 IRS2. NGC1333 IRAS2A has extended features at low surface brightness, and asymmetric extended emission to the east. Then the extended emission for L1448 IRS2 is also more diffuse and does not have as well-defined circumbinary structure like some of the others. However, the larger structure surrounding the protostars may be impacted by spatial filtering given that Tobin et al. (2015a) detected a surrounding structure on larger scales in lower resolution data.

The Class I sources on the whole have little or no extended emission surrounding the components of these multiple systems. The images show this visually in Figure 2, and Table 1 shows that the flux densities for the Gaussian fits and the extended emission from a larger area encompassing the two protostars are comparable. However, some show resolved structure toward one component. Both NGC 1333 IRAS2B and L1448 IRS1 have at least one component that is dominant, with resolved structure in their dust emission. The other Class I binaries appear consistent with point sources, and the components have similar flux densities.

While the close companions were the primary targets, we detected several wide companions in the observed fields. In the field of SVS13A, we detect several additional sources. One source is RAC1999 VLA20 (Rodríguez et al. 1999), located northeast of SVS13A. This source was previously detected by the VLA, but has no counterpart at shorter wavelengths (i.e., mid-infrared and far-infrared) and has been hypothesized to be extragalactic (Tobin et al. 2016b), see Figure 3. The wider companion to SVS13A, often called VLA3 or SVS13A2, is detected (Figure 3), and appears marginally resolved. SVS13B is also detected and resolved as shown in Figure 3). VLA 8 mm imaging of SVS13B indicated that it has a small embedded disk (Segura-Cox et al. 2016), but a larger, resolved structure is detected in the ALMA 1.3 mm data. We also detected L1448 IRS3A in the field of L1448 IRS3B (Figure 4). The small-scale structure of L1448 IRS3A appears to be a resolved disk (Figure 4), consistent with the resolved emission detected in Tobin et al. (2015a). In the field of Per-emb-55 (Figure 5), we also detected Per-emb-8 which appears to have a large extended disk surrounding it (Figure 5). Per-emb-21 was detected in the field of Per-emb-18, but appears unresolved (Figure 6).

The resolved structures around Per-emb-8 and L1448 IRS3A were not ideal for fitting a single Gaussian, so we fit two Gaussians to these sources and list the inner and outer Gaussian fits separately, referring to them as Inner Disk and Outer Disk, in addition to the fit of a single Gaussian in Tables 1 and 2.

### 3.2. Mass Estimates from Dust Continuum

The mass of material found toward individual components of the multiple systems, as well as surrounding all components, can be estimated using the flux density of the dust continuum emission. Under the assumption that the dust emission is optically thin and isothermal, the dust mass can be

calculated with the equation

$$M_{dust} = \frac{D^2 F_\nu}{\kappa_\nu B_\nu(T_{dust})}, \quad (1)$$

where  $D$  is the distance ( $\sim 300$  pc),  $F_\nu$  is the observed flux density,  $B_\nu$  is the Planck function,  $T_{dust}$  is the dust temperature, and  $\kappa_\nu$  is the dust opacity at the observed wavelength.  $T_{dust}$  is assumed to be 30 K, consistent with temperature estimates on  $\sim 100$  AU scales (Whitney et al. 2003) and  $\kappa_\nu$  is 0.899, taken from Ossenkopf & Henning (1994), Table 1 column 5. We then multiply the resulting value of  $M_{dust}$  by 100, assuming the canonical dust to gas mass ratio of 1:100 (Bohlin et al. 1978). We caution that the masses calculated may have systematic uncertainty because opacity will hide some mass, the dust emission is not isothermal and the dust opacity along with the dust to gas mass ratio are uncertain and may vary between components within the same system.

The results from the mass calculations are given in Table 2. A number of sources have total masses greater than  $0.1 M_\odot$ . The mass calculations presented here tend to be about 20% higher than the masses reported for some of the same sources in Tobin et al. (2015a) from observations with CARMA (taking into account the different distances adopted), despite observing at the same wavelength, slightly lower resolution (for CARMA), and making the same assumptions for the mass calculation. The minor discrepancy likely results from a combination of greater absolute flux uncertainty in the CARMA data, better sensitivity to low-surface brightness emission from ALMA, better uv-coverage with ALMA, and less decoherence in the self-calibrated ALMA data.

Most of the close companions have large flux density ratios between them, which could be interpreted as a large circumstellar mass ratio; this ratio offers no information as to the mass ratio between the stellar components and only reflects the compact circumstellar mass. Per-emb-17, EDJ2009-269, and Per-emb-35 have ratios closest to unity, and L1448 IRS1, L1448 NW, Per-emb-12, Per-emb-22, Per-emb-27, Per-emb-33, Per-emb-36, Per-emb-40, Per-emb-44, Per-emb-49, and Per-emb-55 all have circumstellar mass ratios that are less than 0.63. Both Class 0 and Class I systems span a range of circumstellar mass ratios. We note that several cases with large circumstellar mass ratios are in hierarchical and/or higher order systems.

### 3.3. Spectral Indices

Because most of the companions are well-enough resolved to enable their 1.3 mm flux densities to be measured individually, We were able to calculate the spectral index of the emission from 1.3 mm to 9.1 mm. We calculated the spectral index ( $\alpha$ ) using the equation

$$\alpha = \frac{\ln(F_{\nu,1.3mm}) - \ln(F_{\nu,9.1mm})}{\ln(\nu_{1.3mm}) - \ln(\nu_{9.1mm})} \quad (2)$$

and the associated uncertainty using the equation

$$\sigma_\alpha^2 = \left( \frac{1}{\ln(\nu_{1.3mm}) - \ln(\nu_{9.1mm})} \right)^2 \left( \frac{\sigma_{\nu,1.3mm}^2}{F_{\nu,1.3mm}^2} + \frac{\sigma_{\nu,9.1mm}^2}{F_{\nu,9.1mm}^2} \right) \quad (3)$$

following Chiang et al. (2012). We use the 9.1 mm flux densities from Tychoniec et al. (2018b) to calculate  $\alpha$  with respect to the flux densities at 1.3 mm. Because Tychoniec et al. (2018b) attempted to remove the free-free emission that can contribute to the 9.1 mm flux densities, we calculated  $\alpha$  with respect to both the corrected and uncorrected 9.1 mm flux densities. The spectral indices for

the sources are given in Table 1. The statistical uncertainty on  $\alpha$  is generally quite small  $\sim 0.1$  due to the large difference in wavelength between the two bands. We do assume a 10% uncertainty in the flux calibration for each flux density and add this in quadrature to the statistical uncertainty on the flux density. The uncertainty on  $\alpha$  is generally smaller than the range of  $\alpha$  from the corrected and uncorrected flux densities.

Most of the values for  $\alpha$  are between 2 and 3; optically thin thermal dust emission, where the dust opacity spectral index  $\kappa_\nu \propto \nu^\beta$ , is expected to have  $\alpha = 2 + \beta$ . Thus, for thermal dust emission alone (optically thin or partially optically thin), the spectral indices should be  $\geq 2$ ; the spectral index would be 2 for optically thick emission. Most of the values of  $\alpha$  are  $> 2$  even when the 9.1 mm emission was not corrected for free-free emission, thus it is likely that the 9.1 mm mostly reflects dust emission as also found by [Tychoniec et al. \(2018b\)](#). There are some sources for which  $\alpha \sim 2$ , this could indicate that either the properties of the dust grains are such that  $\beta$  is quite small, the dust emission is becoming optically thick, or there is some amount of free-free emission to the 9.1 mm flux density that could not be removed. These three possibilities are difficult to disentangle with the data in-hand, limiting the possible interpretations of these spectral index data. Therefore, the 1.3 mm emission presented here is most likely to *only* reflect dust emission while the 9.1 mm emission might reflect dust and free-free emission.

### 3.4. Molecular Line Kinematics

The dust continuum emission provides crucial evidence of the presence or absence of material surrounding the close binary/multiple stars, which will help with the interpretation of their formation mechanism. However, the continuum data alone are not enough to fully understand how these multiple systems formed. Therefore, we also observed five molecular tracers toward each system along with the dust continuum. We expect that  $\text{C}^{18}\text{O}$  will generally trace the kinematics of the dense circum-multiple material because this line has tended to be the most reliable tracer of protostellar disks ([Ohashi et al. 2014](#); [Yen et al. 2014](#); [Aso et al. 2015](#)). Also,  $^{13}\text{CO}$  should generally trace the circum-multiple material depending ([Takakuwa et al. 2012](#); [Tobin et al. 2012](#)), but we use  $^{13}\text{CO}$  with caution given that it can also trace outflowing gas.  $\text{H}_2\text{CO}$  is also expected to trace the circum-multiple environment because this is a typical high-density tracer (e.g., [Mangum & Wootten 1993](#)), and it has been found to trace the Class 0 disk and inner envelope of L1527 ([Sakai et al. 2014](#)). Similarly, SO has also been found to trace the disk toward some protostars ([Sakai et al. 2014](#); [Yen et al. 2014](#)). However, there are instances where both  $\text{H}_2\text{CO}$  and SO have been shown to trace outflowing material, in addition to circumstellar/multiple material (e.g., [Wakelam et al. 2005](#)). Finally,  $^{12}\text{CO}$  is expected to trace the outflow toward most protostars in the sample given their youth, but  $^{12}\text{CO}$  could trace the disk kinematics of some of the more evolved multiple systems in our sample (e.g., [Simon et al. 2000](#)). The figures showing the molecular line detections toward circum-multiple and circumstellar structures are shown in Figures 7 to 22. The intervals over which the red and blue shifted emission are integrated are given in Table 3.

Due to the short observations toward each source, the S/N is not very high in each channel for these high-angular resolution spectral line maps. Thus, we examine the integrated intensity maps constructed for emission red- and blue-shifted with respect to the line center. The detection rates for the lines vary from source to source, some only have one line detected, whereas others have detections in all five lines. We examine the integrated intensity maps of each molecule, relative to the outflow directions and the extended continuum structure. The larger-scale outflows have previous

characterization of their orientations, when possible, from [Stephens et al. \(2017\)](#), therefore we only show the outflow maps in Appendix A.

### 3.4.1. *Characterization of Kinematics in Multiples*

We use the red- and blue-shifted integrated intensity maps of each molecule to determine whether or not the velocity patterns observed toward the multiple systems reflect rotation, outflow, or an indistinct process. We do this by comparing the orientation of the velocity gradient relative to the outflow direction (and extended continuum if possible). If there is a velocity gradient in the circum-multiple structure, that is within  $30^\circ$  of orthogonal to the outflow direction, we classify it as being consistent with disk rotation. To quantify the relative orientations of the outflow and velocity gradient directions, we measure the position angle of the outflow and velocity gradient and then take the difference. These values are tabulated in Table 4. To measure the outflow position angle, we draw a line bisecting the outflow and measure its position angle. We follow the same procedure for the velocity gradients, but measure this from the emission peaks in the blue- and red-shifted integrated intensity maps tracing rotation, generally  $\text{C}^{18}\text{O}$ . The position angles do have uncertainty and we estimate that this is  $\pm 10^\circ$ .

Molecular line emission is detected with sufficiently high S/N in 12 systems to characterize the kinematics as rotation or not. This classification is most firm for the 9 Class 0 systems with the strongest detections and seven of these Class 0 systems have velocity gradients that indicate rotation in the circum-multiple gas. If we include those with tentative classifications, we find that 8 out of 12 systems are consistent with the circum-multiple emission tracing rotation orthogonal to the outflow direction. The systems classified as indistinct generally have disorganized kinematic structure on the scales and at the sensitivity we observed. Also, certain molecules may better trace different kinematic components of protostellar systems ([Sakai et al. 2014](#), e.g.,). The detection and characterization of the molecular line data are summarized in Table 4. Each source is discussed in more detail in Section 4.1 with respect to the data presented in this paper and to interpret previous results in the context of the new ALMA data.

### 3.4.2. *Detections of Individual Rotating Disks*

In addition to the kinematic structure of circum-multiple material, we were also able to examine the kinematic structure of both some individual circumstellar disks either as part of a close multiple system or as a wide companion. Per-emb-8 shows the clearest example of rotation in all observed molecular lines;  $^{12}\text{CO}$  interestingly shows a combination of rotation and outflow. L1448 IRS3A also shows rotation in all molecular lines and is oriented orthogonal to the position angle of L1448 IRS3B. The individual disks toward Per-emb-35-A and -B appear to have molecular line emission as well, but the line emission is not well-resolved spatially. Only the  $\text{H}_2\text{CO}$  appears to have a clear indication of rotation. The characterization of the observed kinematics from all lines are given in Table 4.

## 4. DISCUSSION

The ALMA 1.3 mm continuum and molecular line emission observed toward the close multiple systems in Perseus dramatically increases our knowledge of the spatial and kinematic structure of dense gas on a few hundred AU scales around these multiple protostar systems. The ALMA dust continuum traces more tenuous emission surrounding the companions as compared to the previous VLA observations. While the extended emission is more diffuse than the compact sources detected

by both the VLA and ALMA, this emission can account for a significant fraction of the mass in the systems. The molecular maps show the gas motion, revealing how well (or not) the motion of the extended dense gas surrounding the protostar(s) is organized. The molecular line maps provide evidence for rotation in several systems, but not universally, as some systems have unclear kinematic structure with the current S/N of the ALMA data. Nevertheless, these ALMA data now enable us to better interpret how multiple star systems form on a case-by-case basis and as an ensemble. We consider each system individually and summarize our findings for the sample as a whole.

#### 4.1. *Individual Systems*

##### 4.1.1. *Class 0 and 0/I Systems*

**Per-emb-2**– The continuum structure is extended with a very smooth surface brightness distribution, in contrast to the VLA data with a central intensity peak toward the protostars, forming a binary system with a separation of  $\sim 24$  AU. Only  $\text{C}^{18}\text{O}$  and  $^{13}\text{CO}$  were detected toward this system, and we detect a clear velocity gradient orthogonal to the outflow direction, as shown in Figure 7. The  $\text{C}^{18}\text{O}$  emission is not fully coincident with the continuum image, possibly due to dust opacity and/or spatial filtering of low-velocity emission near line-center. Nevertheless, the  $\text{C}^{18}\text{O}$  and  $^{13}\text{CO}$  kinematics still exhibit evidence for rotation on the scale of the circumbinary continuum.

**Per-emb-12**– Also known as NGC 1333 IRAS4A, this system is the most massive overall in terms of dust emission out to very large scales. It was also known to be a binary prior to the VANDAM survey with a separation of  $\sim 549$  AU (Looney et al. 2000). The dust emission toward IRAS4A has significant opacity, which prevents tracing kinematics toward the protostars; only some emission around the protostars in  $\text{C}^{18}\text{O}$  and  $^{13}\text{CO}$  is revealed in Figure 8.

**Per-emb-17**– There were detections in multiple lines toward Per-emb-17, and the material surrounding the  $\sim 83$  AU binary system forms a flattened structure in dust continuum that is similarly flat in  $^{13}\text{CO}$  and  $\text{C}^{18}\text{O}$ . The molecular line emission exhibits velocity gradients orthogonal to the outflow direction, see Figure 9. The rotation center of the system is not clearly centered on a particular component, so it is unclear which protostar is more massive.  $\text{H}_2\text{CO}$  and  $\text{SO}$ , however, seem to be more associated with the outflow in this source.  $\text{SO}$  in particular is strong toward the B component and extended along the outflow.

**Per-emb-18**– This source has a flattened structure in the dust continuum surrounding the companions separated by  $\sim 26$  AU and detections in multiple lines. The continuum might be tracing dust emission with high optical depth, given that the emission is not very peaked toward the main pair of protostars. The  $^{13}\text{CO}$ ,  $\text{C}^{18}\text{O}$ ,  $\text{SO}$ , and  $\text{H}_2\text{CO}$  trace velocity gradients orthogonal to the outflow direction, see Figure 10. The fact that all molecules have gradients in the same direction lends confidence to interpreting the kinematics as rotation.

**Per-emb-22**– Also known as L1448 IRS2, this binary system has a separation of  $\sim 225$  AU. Continuum emission was mainly detected toward individual components, with some emission in between, exhibiting an apparent ‘bridge’ between them. The molecular lines have evidence of velocity gradients orthogonal to the outflow (Figure 11), but much of the molecular line emission appears to be filtered out and/or have very low surface brightness. Tobin et al. (2015a) previously found evidence for velocity gradients/rotation using combined CARMA and SMA data that had lower resolution, in addition to a larger circumbinary structure.

**Per-emb-27**– Also known as NGC 1333 IRAS2A, this system does not have much material surrounding the  $\sim 186$  AU binary, but there is some extended material associated with the brighter source. There is weak evidence for a velocity gradient in  $\text{C}^{18}\text{O}$  on scales larger than the binary system. SO is associated with the outflow, but  $\text{H}_2\text{CO}$  is compact toward the brighter component with a small extension toward the companion, see Figure 12.

**Per-emb-33/L1448 IRS3B**– This source was shown in Tobin et al. (2016a) to have clear velocity gradients associated with its extended circumbinary material in  $^{13}\text{CO}$ ,  $\text{C}^{18}\text{O}$  and  $\text{H}_2\text{CO}$ . The separations of the companions from Per-emb-33-A are  $\sim 79$  and  $\sim 238$  AU. Despite being published previously, we show this source for the sake of comparison to the full sample (Figure 13).

**L1448 IRS3C**– The two companions in this system are separated by just  $\sim 75$  AU, and they appear blended in the image. However, the emission toward each component is measured using a two component Gaussian fit. There is low-level dust continuum emission surrounding the two blended protostars, and the circumbinary material also shows a velocity gradient in  $\text{C}^{18}\text{O}$  orthogonal to the outflow, see Figure 14.

**Per-emb-44**– Also known as SVS 13A, this binary system has a companion separation of  $\sim 90$  AU and is one of the most prominent protostars within NGC1333. The 1.3 mm continuum also shows a 1-armed spiral pattern, almost as prominent as that of L1448 IRS3B. Both  $^{13}\text{CO}$  and  $\text{C}^{18}\text{O}$  are detected toward this protostar and exhibit velocity gradients that are at least partially orthogonal to the outflow, see Figure 15. This source might be viewed more face-on making rotation harder to distinguish in this complex environment. The  $\text{C}^{18}\text{O}$  emission also follows the spiral through multiple velocity channels. Furthermore, both SO and  $\text{H}_2\text{CO}$  are detected at smaller radii near the close pair and may also show a velocity gradient, but it is uncertain due to blending. This protostar was previously known to have a close companion (Anglada et al. 2004), and the original study indicated that the disk around the western companion (Per-emb-44-B; VLA 4A) was not very prominent given its low flux density relative to the eastern component (Per-emb-44-A; VLA 4B) at a wavelength of 7 mm. However, their masses (flux densities) differ by only a factor of 1.6 at 1.3 mm, which may have more to do with either the amount of large grains and/or variable free-free emission because Anglada et al. (2004) used data at a wavelength of 7 mm from the VLA. However, Tychoniec et al. (2018c) also finds that the 9 mm flux densities (with estimated free-free contribution removed) have a flux ratio of 2.8, and the spectral indices are quite different  $\sim 2.3$  for the eastern component and  $\sim 3$  for the western component. This could indicate more large grains in the eastern source to explain the increased flux density, or the 1.3 mm is optically thick and the 8 mm emission is less opaque, enabling more dust emission to be detected.

#### 4.1.2. Class I & II Systems

**Per-emb-36 (NGC 1333 IRAS2B)** – The two sources detected toward Per-emb-36 are marginally resolved in the ALMA 1.3 mm data with a separation of  $\sim 93$  AU, and it has multiple detected emission lines (Figure 16). However, the line emission does not obviously trace velocity gradients across the source, and the emission is mainly found west of the protostars rather than around them.

**Per-emb-35** – These protostars are separated by  $\sim 572$  AU, and they are the source of an S-shaped outflow detected by *Spitzer* (Gutermuth et al. 2008). These sources do not have obvious dust continuum surrounding the compact continuum sources, but we cannot rule-out diffuse circumbinary emission below our detection limits.  $\text{H}_2\text{CO}$  and SO are strongly detected toward both of the protostars

and may show evidence of velocity gradients orthogonal to their outflow directions (Figure 17). Furthermore, there appears to be emission in these molecules between the two protostars. Both protostars are driving outflows, and they appear parallel as observed in the plane of the sky.  $^{13}\text{CO}$  is detected toward both sources, but it is not obviously tracing rotation, and  $\text{C}^{18}\text{O}$  is only weakly detected, also see Figure 17.

**Per-emb-40** – Only the primary component of this system is well-detected, but the companion is tentatively detected. The molecules  $^{13}\text{CO}$  and  $\text{C}^{18}\text{O}$  are only weakly detected (Figure 18).  $^{13}\text{CO}$  does have blue- and red-shifted components, but not obviously tracing rotation.

**L1448 IRS1** – This protostar appears to be the most evolved source in L1448, and it is detectable at visible wavelengths. The separation of the two protostars is  $\sim 427$  AU. Unlike the other protostellar systems, the rotation in L1448 IRS1 is traced by  $^{12}\text{CO}$  that is extended toward the companion, see Figure 19. In this particular case,  $^{12}\text{CO}$ , is not tracing outflowing emission but rather the disk because of its advanced evolutionary state. We know this because the scattered light nebula from this source (Foster & Goodman 2006), which is an alternative indicator of the outflow direction, is oriented orthogonal to the velocity gradient in  $^{12}\text{CO}$ .

**EDJ2009-269** – This system is a likely Class II binary in Perseus, separated by  $\sim 157$  AU. Its only detected emission line is  $^{12}\text{CO}$  toward one of the protostars (Figure 20). In this more-evolved system, the  $^{12}\text{CO}$  also appears to trace kinematics of gas toward the individual circumstellar disks rather than outflowing material.

**Per-emb-48, Per-emb-49, and Per-emb-55** – These protostars do not show strong evidence for molecular line emission surrounding the companion stars, thus we cannot examine whether or not there are velocity gradients in the circum-multiple emission. These are all Class I systems and may simply have a much smaller reservoir of circumbinary material, and/or the molecular line emission could not be detected with our uv-coverage and/or sensitivity. Per-emb-55, however, does appear to have an outflow associated with it in  $^{12}\text{CO}$  emission, see Appendix Figure 24.

#### 4.1.3. *Wide Companions with Disks*

**L1448 IRS3A** – This is the wide companion to L1448 IRS3B, separated by  $7''.3$  ( $\sim 2195$  AU), and has extended dust emission with disk-like morphology. The protostar exhibits a weak outflow in  $^{12}\text{CO}$ , but rotation in all the other observed lines, see Figure 21.

**Per-emb-8** – This protostar is clearly detected with extended dust emission that shows signatures of rotation from the molecular line emission (Figure 22). It is separated from Per-emb-55 by  $\sim 2867$  AU. Per-emb-8 was previously identified as a disk candidate by Segura-Cox et al. (2016), but with a very different position angle than is observed with ALMA. Since this source appears to have strong, extended free-free emission (Tychoniec et al. 2018a), the geometric parameters from the VLA data may not solely trace the dusty disk.

### 4.2. *The Origin of Close Protostellar Multiples*

The ALMA continuum and molecular line maps are key to determining the most likely origin of the multiple star systems. Systems that have formed via disk fragmentation are expected to have circum-multiple dust emission and this circum-multiple material should be rotating in an organized manner. Furthermore, if fragmentation happened in a disk, the disk should be larger than the separation of the companions. Systems that result from turbulent fragmentation have no such expectations for their circum-multiple emission and may not have well-organized kinematics surrounding the system.

We discuss our interpretation on the relative frequency of these mechanisms based on our ALMA molecular line and continuum data.

#### 4.2.1. *The Likelihood of Disk Fragmentation*

The ALMA observations of close multiple protostar systems reveal several features that were previously unclear from the VLA-only dataset. First, the continuum emission from extended circumbinary (or triple) material is detected in 9 out of the 18 observed sources. The Class 0s and most deeply embedded Class Is have the highest tendency for circum-multiple dust continuum. Furthermore, this circum-multiple continuum emission is almost always extended orthogonal to the outflows (L1448 IRS3B, L1448 IRS3C, L1448 IRS2, Per-emb-12, Per-emb-17, Per-emb-18), barring a few cases that appear to have inclinations that are nearly face-on (SVS13A, Per-emb-2). Second, the molecular line emission detected toward these protostars and their circum-multiple disks strongly tends to have velocity gradients orthogonal to the outflow direction (Per-emb-2, L1448 IRS3B, L1448 IRS3C, L1448 IRS2, Per-emb-17, Per-emb-18, SVS13A, L1448 IRS1). The line emission is spatially coincident with the circum-multiple dust emission (taking into account the possible dust opacity and spatial filtering in some sources), and the velocity gradients orthogonal to the outflows on these scales are interpreted as rotation because the mass of the protostar and its disk are dominant at these scales ( $< 500$  AU) and do not appear to be significantly confused with large-scale effects in the clouds.

Therefore, it is clear that for many of the youngest multiple systems we have circum-multiple dust emission oriented in a manner that is consistent with a disk, and we detect molecular line kinematics that are consistent with rotation on the same scale as the circum-multiple material. We detail the molecular line detections and their likely kinematic origin for each source in Table 4. The observational results of rotating, circum-multiple gas align with the expectations for companion formation via disk fragmentation. Direct evidence for the circum-multiple material in only the younger sources makes sense, because as they evolve, the circum-multiple material is accreted rapidly (Bate 2018). Thus, about 7 protostars in the sample appear to have recently undergone disk fragmentation (those listed above with velocity gradients orthogonal to the outflow and extended circum-multiple mass). Many of the Class I close systems without circum-multiple dust or gas may have formed earlier and/or consumed/dispersed their surrounding mass. The widest systems that appear convincingly consistent with disk fragmentation are Per-emb-22 (225 AU) and Per-emb-33 (79, 238 AU) and there is circum-multiple continuum detected in both cases. L1448 IRS1 is possibly consistent with disk fragmentation, but the companion is at a wider separation (427 AU) and the disk would have had to be quite large initially to form the companion, unless there was a three-body interaction that moved the companion to a larger orbit (Reipurth & Mikkola 2012). This would then require that L1448 IRS1-A has an unresolved companion.

These ALMA observations provide important evidence for the possibility of fragmentation via gravitational instability in these systems. Additional follow-up with higher S/N will be required to confirm that these apparent disks are rotationally supported and to determine the outer radius of the Keplerian disk, ensuring that it encompasses the companion. The short observations presented here do not have the S/N to robustly fit a rotation curve that can distinguish Keplerian rotation from other velocity profiles. Therefore, at this point, we can conclude that there is evidence in favor of these systems forming via fragmentation in a gravitationally unstable disk, like L1448 IRS3B. There is rotation, circum-multiple dust, and the companions are most often orthogonal to the outflow and within the circum-multiple material.

#### 4.2.2. Evidence for Turbulent Fragmentation in Some Systems

There are a few systems where disk fragmentation is not obviously consistent with the observations and turbulent fragmentation is more likely (i.e., Per-emb-27; Tobin et al. 2015b). Per-emb-27 in particular has some evidence for a velocity gradient in C<sup>18</sup>O but not in other tracers. H<sub>2</sub>CO in fact appears very centrally peaked toward Per-emb-27-A and may be tracing the hot corino (e.g., Taquet et al. 2015). Furthermore, the disk toward Per-emb-27-A appears to be very small, ~10 AU in radius (Segura-Cox et al. 2018). Thus, Per-emb-27 seems unlikely to have any characteristics that make disk fragmentation a likely possibility for this system.

The source Per-emb-12 (NGC 1333 IRAS4A) is borderline for consideration as a close companion with its ~549 AU separation. We see a significant amount of material surrounding the two sources, but this is not clearly organized as a disk and is perhaps more likely a circumbinary envelope. The outflows from these two sources are roughly aligned, indicating that envelope rotation could have played a role in their formation, but the kinematics are unclear because the line emission is so complex due to the high opacity and spatial filtering that we cannot clearly say if there is organized rotation or if the inner envelope kinematics appear random.

The source Per-emb-36 (NGC 1333 IRAS2B) has extended gas emission surrounding it, but not obvious circum-multiple dust emission. Some of the gas appears off to one side and the companion is located toward the western side where much of the gas emission tends to originate. The kinematic structure of this system is unclear and the outflow is quite wide (Plunkett et al. 2013). Thus, we cannot firmly put this binary system in either category. Given that Per-emb-36 is a Class I protostar, it is possible that much of the original gas has been accreted and there is no longer a prominent circum-multiple disk. This could be a case of turbulent fragmentation, but it is hard to be more definitive with the more-evolved state of Per-emb-36.

Per-emb-35 is another case that is not obviously disk fragmentation given its wide separation of 572 AU. However, unlike Per-emb-12, it is much less embedded and the continuum emission is dominated by the compact circumstellar components that may exhibit rotation in some molecular species (Figure 17). While there is not much evidence for circumbinary material, the outflows (and possibly rotation axes traced by molecular lines) appear roughly parallel. Furthermore, the outflows are inclined in the same direction with respect to the plane of the sky. This case is also not obviously turbulent fragmentation or disk fragmentation. On the other hand the fragmentation mechanism in this system could be related to the overall rotation of the envelope (e.g., Burkert & Bodenheimer 1993), despite this mechanism not being favored. However, turbulent fragmentation does not rule-out some outflows being parallel, just that the distribution over a larger sample should be random.

#### 4.2.3. Which is the Most Common Mechanism?

In total, we can make reasonably strong statements about the formation mechanisms for 9 out of the 17 protostars in our sample based on the extended dust emission and gas kinematics. Seven out of the 9 (Per-emb-2, L1448 IRS3B, L1448 IRS3C, L1448 IRS2, Per-emb-17, Per-emb-18, SVS13A) appear to be consistent with fragmentation of a gravitationally unstable disk given their observed morphologies and velocity gradients. There are only two systems (Per-emb-12, Per-emb-27) for which we can state with reasonable confidence that they are inconsistent with disk fragmentation and that turbulent fragmentation is more likely. With the caveats of having a large separation and only a hint of rotation in <sup>12</sup>CO we could add L1448 IRS1 to the disk fragmentation group. Then Per-emb-36 and

Per-emb-35 could also be added to the turbulent fragmentation group, bringing the total to 8 systems likely forming via disk fragmentation to 4 systems likely forming via turbulent fragmentation. The raw numbers indicate that for multiples on scales  $<600$  AU,  $\sim 67\%$  form via disk fragmentation and  $\sim 33\%$  form via turbulent fragmentation. If we only consider systems with  $<300$  AU separations, more in line the sizes of disks, then there are a total of 10 systems with only 2 systems inconsistent with disk fragmentation. The smaller separations systems, further indicates that the closer systems may be more frequently formed via disk fragmentation. However, these percentages obviously represent small number statistics making, prohibiting us from making a strong, general conclusion on the typical origin of close multiple systems.

A dominant contribution from turbulent fragmentation would not necessarily result in the presence of circumbinary disks within which the companions are embedded, and outflows would not tend to appear aligned orthogonal to the companion position angles and/or velocity gradients.

There is not currently a clear prediction for the relative fractions from theory/simulations. [Offner et al. \(2010\)](#) indicate that most close companions should result from turbulent fragmentation because radiative heating of the protostellar disk should suppress fragmentation. On the other hand, the simulations from [Bate \(2018\)](#) include radiative feedback and do find disk fragmentation, but a study of the relative population of companions in different ranges of separations has not been conducted. However, it should be noted that [Offner et al. \(2010\)](#) and [Bate \(2012\)](#) employ different initial cloud conditions (turbulence and volume density) and different assumptions for the radiative heating. Both of these factors are likely to influence the fragmentation on cloud and disk scales in both simulations. Even in the presence of radiative heating, fragmentation can still occur for systems with total masses (star+disk) of  $>1 M_{\odot}$  ([Kratter et al. 2008, 2010](#)). The [Offner et al. \(2010\)](#) simulations may be underpredicted disk fragmentation because most of the systems in that simulation were  $<1 M_{\odot}$ , and the different treatment of radiative heating in [Bate \(2012, 2018\)](#) could overpredict fragmentation in this mass range.

While we suggest that our results favor disk fragmentation as a formation mechanism for these systems, there is an inescapable caveat. Even if the disks are Keplerian, there remains the possibility that initially widely separated companions could have migrated closer together ([Offner et al. 2010; Sadavoy & Stahler 2017](#)). In the process, the original disks may have been destroyed and a new disk reformed around the companions in the same orbital plane. While the outflows could be misaligned initially ([Offner et al. 2016](#)), they could be brought into alignment and appear as a single outflow as the protostars accrete from the disk surrounding them. However, there is not evidence for past multiple outflows in different directions for the systems where we would have the possibility of determining this. But, the timescales over which we could detect remnant outflows might be too short. Further study of circum-multiple material surrounding systems formed via initially turbulent fragmentation may provide clues to more uniquely distinguish between primordial disk fragmentation and turbulent fragmentation with a re-formed disk. Therefore, our main result finding that 8 out of 12 sources are consistent with disk fragmentation could be rephrased to say that 66% is an upper limit on the frequency disk fragmentation for the production of close multiples.

#### 4.3. *Non-detections of Companions*

In our ALMA follow-up of the VLA-detected close multiples, we detect the companions in 12 out of 15 multiple systems that we were able to resolve. We left Per-emb-2 and Per-emb-18 out of these numbers because it is not possible to resolve their companions in these observations. All Class 0

companions are detected, and only the Class I companions have some non-detections. However, in the case of the non-detections, we do marginally detect one of the components in Per-emb-40, Per-emb-55 has a tentative detection toward the companion position. Finally, Per-emb-48 could also not be self-calibrated, reducing its likelihood to detect the companion.

The fact that most of the non-detections were more-evolved Class I systems makes sense given that the VLA is detecting a combination of dust and free-free emission in most cases. The non-detected component of Per-emb-48 was Per-emb-48-B; Tychoniec et al. (2018) detected Per-emb-48-B with a declining spectral index from 6.4 cm to 8 mm, consistent with gyro-synchrotron from a stellar corona. Per-emb-55-B, the very tentative detection, had a spectral index that was rising (0.9) but more flat than expected from dust emission alone ( $\geq 2$ ). Assuming a spectral index of 3 (implicitly assumes a dust opacity spectral index of 1), we extrapolate the 9 mm flux density of 0.07 mJy to 1.3 mm. In order to have a flux density consistent with the observations, a flux density of less than 1 mJy,  $\sim 95\%$  of the 9 mm emission from Per-emb-55-B must be from free-free emission. Tychoniec et al. (2018b) found that 79% of the 9 mm emission was from free-free emission, this would also point to the spectral index of the source emission being shallower than 3. Per-emb-40-B was quite faint and also appeared to have a declining spectral index in 8 mm to 1 cm; the 4.1 cm and 6.4 cm were much fainter than expected, possibly due to source variability (e.g., Dzib et al. 2013). However, Per-emb-40-B has extended dust toward it, so it is probably real, but not detected at our level of sensitivity.

The faintness of companions toward some of these close Class I protostars is consistent with the results of Harris et al. (2012). While that study examined Class II stellar systems, they found that the systems with close separations ( $< 300$  AU) had a factor of 5 lower millimeter emission compared to single systems and systems with  $> 300$  AU separations. Moreover, the primary was always brighter than the secondary in the cases where both components of the system were detected at millimeter wavelengths. Thus, evolution may drive the companion(s) to be significantly fainter than the primary, and the flux density of close ( $< 300$  AU) systems to be lower than more widely separated and/or single systems.

It is also worth discussing the cases of some other companion sources reported toward protostars in Perseus. A possible new companion source was reported near Per-emb-12 (NGC 1333 IRAS4A), referred to as A3 in Santangelo et al. (2015), with a 1.3 mm flux density of 187 mJy. This source A3 is not detected with the VLA in VANDAM nor with our ALMA 1.3 mm data; we only detect the two known protostars and the extended emission around them. Santangelo et al. (2015) also did not detect this source at a wavelength of 3 mm. This case of A3 toward Per-emb-12 is very similar to the case of the companions (denoted MM2 and MM3) around Per-emb-27 (NGC 1333 IRAS2A) reported by Maury et al. (2014) from PdBI observations. These companions were not detected by the VLA, CARMA, or the SMA, as detailed in Tobin et al. (2015b) or by the more sensitive ALMA data presented here. It is most likely that A3 toward Per-emb-12 and MM2 and MM3 toward Per-emb-27 are either artifacts from the deconvolution process and/or additional noise resulting from dynamic range limitations of the PdBI as was previously discussed in Tobin et al. (2015b).

In a similar vein, there have been hypotheses put forward that some clearly detected continuum sources were features produced by outflow interactions (Maury et al. 2010, 2012). However, further study over the past several years has found that, the continuum features that were suggested to be outflow knots in VLA 1623, are definitively real protostars (Murillo & Lai 2013; Murillo et al. 2013;

Sadavoy et al. 2018; Harris et al. 2018). The other cases where continuum sources were suggested to be outflow features (i.e., L1448-mm, NGC 1333 IRAS2A, NGC 1333 IRAS4A, Maury et al. 2010, 2014; Santangelo et al. 2015) seem to be artifacts in those data given their lack of detection here with ALMA and in other works at the same and other wavelengths (Tobin et al. 2015b,a).

While it seems unlikely that outflow features are significantly contributing to the detection of false companions, we note that none of the companions without detections are found along the outflow direction. Moreover, the host protostars of the three non-detections are not driving prominent outflows as viewed from the ALMA  $^{12}\text{CO}$  data. Therefore it seems unlikely that companions are being mimicked by outflow features in our case.

We had an 80% detection rate with ALMA toward the VLA-detected close multiples in Perseus; 100% for the Class 0s and 62.5% for the Class Is. The Class I non-detections based on the VANDAM survey are likely to be real companions but were below our detection limits. For these sources in particular, it might be useful to search for their companions in the near-infrared since they are observed toward sources that are not highly embedded. Thus, we can conclude that VLA-detected companions are quite robust.

## 5. CONCLUSIONS

We have conducted ALMA observations toward 17 VLA-detected proto-multiple systems from the VANDAM survey that are separated by less than 600 AU. We observed these systems in dust continuum at 1.3 mm and the  $^{12}\text{CO}$ ,  $^{13}\text{CO}$ ,  $\text{C}^{18}\text{O}$ ,  $\text{SO}$ , and  $\text{H}_2\text{CO}$  molecular lines, enabling us to examine the circumbinary environments. Our main results are as follows:

- Of the 15 companions that could be resolved in our observations, we detect 12 confidently, with tentative detections for 2 additional sources. We conclude that the VANDAM multiplicity detections from Tobin et al. (2016b) had very high reliability. Though they were not the focus of this study, we also detected all wide companions in the higher-order systems around L1448 IRS3B, Per-emb-55, and Per-emb-44.
- We detect circum-multiple dust emission in 8 out of the 9 deeply embedded Class 0 sources in the sample, but none in the remaining 8 more-revealed Class I systems. For the sources that are closer to edge-on, this material is oriented orthogonal to the outflow direction and the companion stars are embedded within the circum-multiple material. This is consistent with the expectations for their formation within a circumbinary/multiple disk.
- We detect molecular line emission associated with the circum-multiple material in 12 systems (all Class 0 systems and 3 out of 8 Class I systems). The molecular lines with discernible velocity gradients were orthogonal to the outflow directions in 8 out of 12 cases (EDJ2009-269 had too tentative of a detection in  $^{12}\text{CO}$ ). Velocity gradients orthogonal to the outflow on these scales (<600 AU) are most likely due to rotation. Therefore, 8/12 systems are consistent with disk fragmentation and 4/12 appear inconsistent with disk fragmentation. However, the overall numbers are small and may not reflect a general ratio for the origin of close companions.
- Most of the less-embedded Class I systems in our sample do not show circumbinary dust or gas emission. These systems are likely near the end point of their evolution where the circum-multiple disk is mostly accreted or dispersed.

- We identified two additional strong disk candidates, L1448 IRS3A and Per-emb-8. Both show extended dust emission and have molecular line emission that is consistent with rotation. Per-emb-8 now has a better defined position angle compared to what was known previously from the VLA.

We acknowledge fruitful discussions with D. Harsono, P. Sheehan, P. Hennebelle, and N. Reynolds. We also thank the anonymous referee for comments that improved the quality of the manuscript. J.J.T. acknowledges support from NSF grant AST-1814762, the Homer L. Dodge Endowed Chair, and grant 639.041.439 from the Netherlands Organisation for Scientific Research (NWO). This paper makes use of the following ALMA data: ADS/JAO.ALMA#2013.1.00031.S. Z.-Y.L. is supported in part by NSF AST-1616636 and AST-1716259 and NASA NNX14AB38G. ALMA is a partnership of ESO (representing its member states), NSF (USA) and NINS (Japan), together with NRC (Canada), NSC and ASIAA (Taiwan), and KASI (Republic of Korea), in cooperation with the Republic of Chile. The Joint ALMA Observatory is operated by ESO, AUI/NRAO and NAOJ. The National Radio Astronomy Observatory is a facility of the National Science Foundation operated under cooperative agreement by Associated Universities, Inc. This research made use of APLpy, an open-source plotting package for Python hosted at <http://aplpy.github.com>. This research made use of Astropy, a community-developed core Python package for Astronomy (Astropy Collaboration, 2013) <http://www.astropy.org>.

*Facility:* ALMA,

*Facility:* VLA

*Software:* Astropy (<http://www.astropy.org>; [Astropy Collaboration et al. 2018](#); [Greenfield et al. 2013](#)), APLpy (<http://aplpy.github.com>; [Robitaille & Bressert 2012](#)), CASA (<http://casa.nrao.edu>; [McMullin et al. 2007](#)), The IDL Astronomy User's Library (<https://idlastro.gsfc.nasa.gov/>)

## APPENDIX

### A. OUTFLOW OBSERVATIONS

Our observations toward the Perseus multiple systems also encompassed  $^{12}\text{CO}$ , which typically traces outflowing gas toward protostars. We detected outflow signatures toward 13 out of the 17 protostars observed. These detections are shown in Figures 23, 24, & 25. Of the remaining 4 systems that do not appear to have outflows traced by  $^{12}\text{CO}$ , rotation in the disk was found toward L1448 IRS1 (Figure 19), two traced the continuum disk without a clear velocity gradient (Per-emb-48, EDJ2009-269; Figures 20), and one was not detected (Per-emb-49). In most cases, the close multiples only have one outflow that is clearly distinguished, there are a few exceptions, however. Per-emb-12 shows two approximately parallel outflows, Per-emb-27 shows two orthogonal outflows, and Per-emb-35 shows approximately parallel outflows.

### B. COMPANION PROTOSTAR SEPARATION DISTRIBUTIONS

The recently revised distance of  $\sim 300$  pc to the Perseus molecular cloud ([Zucker et al. 2018](#); [Ortiz-León et al. 2018](#)) has resulted in the angular separations of the detected multiple systems corresponding to larger physical separations. We have generated a revised separation distribution using the updated distance for all the the combined sample, and the classes individually and plot the

distributions in Figure 26. We have provided the updated separations in Table 5, 6, and 7. The rest of the information contained in the tables is the same as in Tobin et al. (2016b).

## REFERENCES

- Adams, F. C., Ruden, S. P., & Shu, F. H. 1989, *ApJ*, 347, 959
- André, P., Ward-Thompson, D., & Barsony, M. 1993, *ApJ*, 406, 122
- Anglada, G., Rodríguez, L. F., Osorio, M., et al. 2004, *ApJL*, 605, L137
- Aso, Y., Ohashi, N., Saigo, K., et al. 2015, *ApJ*, 812, 27
- Astropy Collaboration, Price-Whelan, A. M., Sipőcz, B. M., et al. 2018, *The Astropy Project: Building an Open-science Project and Status of the v2.0 Core Package*, , , arXiv:1801.02634
- Bate, M. R. 2012, *MNRAS*, 419, 3115
- . 2018, *MNRAS*, 475, 5618
- Bohlin, R. C., Savage, B. D., & Drake, J. F. 1978, *ApJ*, 224, 132
- Bonnell, I. A., & Bate, M. R. 1994, *MNRAS*, 269, L45
- Brown, D. W., Chandler, C. J., Carlstrom, J. E., et al. 2000, *MNRAS*, 319, 154
- Burkert, A., & Bodenheimer, P. 1993, *MNRAS*, 264, 798
- Chen, X., Arce, H. G., Zhang, Q., et al. 2013, *ApJ*, 768, 110
- Chiang, H., Looney, L. W., & Tobin, J. J. 2012, *ApJ*, 709, 470
- Connelley, M. S., Reipurth, B., & Tokunaga, A. T. 2008, *AJ*, 135, 2526
- Duchêne, G., Bontemps, S., Bouvier, J., et al. 2007, *A&A*, 476, 229
- Duchêne, G., & Kraus, A. 2013, *ARA&A*, 51, 269
- Dunham, M. M., Stutz, A. M., Allen, L. E., et al. 2014, *Protostars and Planets VI*, 195
- Dunham, M. M., Offner, S. S. R., Pineda, J. E., et al. 2016, *ApJ*, 823, 160
- Duquennoy, A., & Mayor, M. 1991, *A&A*, 248, 485
- Dzib, S. A., Loinard, L., Mioduszewski, A. J., et al. 2013, *ApJ*, 775, 63
- Fernández-López, M., Arce, H. G., Looney, L., et al. 2014, *ApJL*, 790, L19
- Foster, J. B., & Goodman, A. A. 2006, *ApJL*, 636, L105
- Greenfield, P., Robitaille, T., Tollerud, E., et al. 2013, *ascl:1304.002*
- Gutermuth, R. A., Myers, P. C., Megeath, S. T., et al. 2008, *ApJ*, 674, 336
- Harris, R. J., Andrews, S. M., Wilner, D. J., & Kraus, A. L. 2012, *ApJ*, 751, 115
- Harris, R. J., Cox, E. G., Looney, L. W., et al. 2018, *ArXiv e-prints*, arXiv:1805.08792
- Hirota, T., Honma, M., Imai, H., et al. 2011, *PASJ*, 63, 1
- Hirota, T., Bushimata, T., Choi, Y. K., et al. 2008, *PASJ*, 60, 37
- Kirk, H., Dunham, M. M., Di Francesco, J., et al. 2017, *ApJ*, 838, 114
- Kratter, K. M., Matzner, C. D., & Krumholz, M. R. 2008, *ApJ*, 681, 375
- Kratter, K. M., Matzner, C. D., Krumholz, M. R., & Klein, R. I. 2010, *ApJ*, 708, 1585
- Lee, K. I., Dunham, M. M., Myers, P. C., et al. 2016, *ApJL*, 820, L2
- Looney, L. W., Mundy, L. G., & Welch, W. J. 2000, *ApJ*, 529, 477
- Mangum, J. G., & Wootten, A. 1993, *ApJS*, 89, 123
- Maury, A., Ohashi, N., & André, P. 2012, *A&A*, 539, A130
- Maury, A. J., André, P., Hennebelle, P., et al. 2010, *A&A*, 512, A40
- Maury, A. J., Belloche, A., André, P., et al. 2014, *A&A*, 563, L2
- McKee, C. F., & Ostriker, E. C. 2007, *ARA&A*, 45, 565
- McMullin, J. P., Waters, B., Schiebel, D., Young, W., & Golap, K. 2007, in *Astronomical Society of the Pacific Conference Series*, Vol. 376, *Astronomical Data Analysis Software and Systems XVI*, ed. R. A. Shaw, F. Hill, & D. J. Bell, 127
- Murillo, N. M., & Lai, S.-P. 2013, *ApJL*, 764, L15
- Murillo, N. M., Lai, S.-P., Bruderer, S., Harsono, D., & van Dishoeck, E. F. 2013, *A&A*, 560, A103
- Offner, S. S. R., Dunham, M. M., Lee, K. I., Arce, H. G., & Fielding, D. B. 2016, *ApJL*, 827, L11
- Offner, S. S. R., Kratter, K. M., Matzner, C. D., Krumholz, M. R., & Klein, R. I. 2010, *ApJ*, 725, 1485

- Ohashi, N., Saigo, K., Aso, Y., et al. 2014, *ApJ*, 796, 131
- Ortiz-León, G. N., Loinard, L., Dzib, S. A., et al. 2018, *ArXiv e-prints*, arXiv:1808.03499
- Ossenkopf, V., & Henning, T. 1994, *A&A*, 291, 943
- Padoan, P., & Nordlund, Å. 2002, *ApJ*, 576, 870
- Pineda, J. E., Offner, S. S. R., Parker, R. J., et al. 2015, *Nature*, 518, 213
- Plunkett, A. L., Arce, H. G., Corder, S. A., et al. 2013, *ApJ*, 774, 22
- Raghavan, D., McAlister, H. A., Henry, T. J., et al. 2010, *ApJS*, 190, 1
- Reipurth, B., & Mikkola, S. 2012, *Nature*, 492, 221
- Robitaille, T., & Bressert, E. 2012, *APLpy: Astronomical Plotting Library in Python, Astrophysics Source Code Library*, , , ascl:1208.017
- Rodríguez, L. F., Anglada, G., & Curiel, S. 1999, *ApJS*, 125, 427
- Rodríguez, L. F., Reipurth, B., Raga, A. C., & Cantó, J. 1998, *RMxAA*, 34, 69
- Sadavoy, S. I., & Stahler, S. W. 2017, *MNRAS*, 469, 3881
- Sadavoy, S. I., Myers, P. C., Stephens, I. W., et al. 2018, *ArXiv e-prints*, arXiv:1804.05968
- Sakai, N., Oya, Y., Sakai, T., et al. 2014, *ApJL*, 791, L38
- Santangelo, G., Codella, C., Cabrit, S., et al. 2015, *A&A*, 584, A126
- Segura-Cox, D. M., Harris, R. J., Tobin, J. J., et al. 2016, *ApJL*, 817, L14
- Segura-Cox, D. M., Looney, L. W., Tobin, J. J., et al. 2018, *ArXiv e-prints*, arXiv:1808.10438
- Simon, M., Dutrey, A., & Guilloteau, S. 2000, *ApJ*, 545, 1034
- Stamatellos, D., & Whitworth, A. P. 2009, *MNRAS*, 392, 413
- Stephens, I. W., Dunham, M. M., Myers, P. C., et al. 2017, *ApJ*, 846, 16
- Storm, S., Mundy, L. G., Fernández-López, M., et al. 2014, *ApJ*, 794, 165
- Takakuwa, S., Kiyokane, K., Saigo, K., & Saito, M. 2015, *ApJ*, 814, 160
- Takakuwa, S., Saito, M., Lim, J., et al. 2012, *ApJ*, 754, 52
- Takakuwa, S., Saito, M., Saigo, K., et al. 2014, *ApJ*, 796, 1
- Taquet, V., López-Sepulcre, A., Ceccarelli, C., et al. 2015, *ApJ*, 804, 81
- Tobin, J. J., Hartmann, L., Chiang, H.-F., et al. 2012, *Nature*, 492, 83
- . 2011, *ApJ*, 740, 45
- Tobin, J. J., Bergin, E. A., Hartmann, L., et al. 2013, *ApJ*, 765, 18
- Tobin, J. J., Looney, L. W., Wilner, D. J., et al. 2015a, *ApJ*, 805, 125
- Tobin, J. J., Dunham, M. M., Looney, L. W., et al. 2015b, *ApJ*, 798, 61
- Tobin, J. J., Kratter, K. M., Persson, M. V., et al. 2016a, *Nature*, 538, 483
- Tobin, J. J., Looney, L. W., Li, Z.-Y., et al. 2016b, *ApJ*, 818, 73
- Tychoniec, L., Tobin, J. J., Karska, A., et al. 2018a, *ApJ*, 852, 18
- . 2018b, *ArXiv e-prints*, arXiv:1806.02434
- . 2018c, *ArXiv e-prints*, arXiv:1806.02434
- Wakelam, V., Ceccarelli, C., Castets, A., et al. 2005, *A&A*, 437, 149
- Whitney, B. A., Wood, K., Bjorkman, J. E., & Wolff, M. J. 2003, *ApJ*, 591, 1049
- Yen, H.-W., Takakuwa, S., Ohashi, N., et al. 2014, *ApJ*, 793, 1
- Zucker, C., Schlafly, E. F., Green, G. M., et al. 2018, *ArXiv e-prints*, arXiv:1803.08931

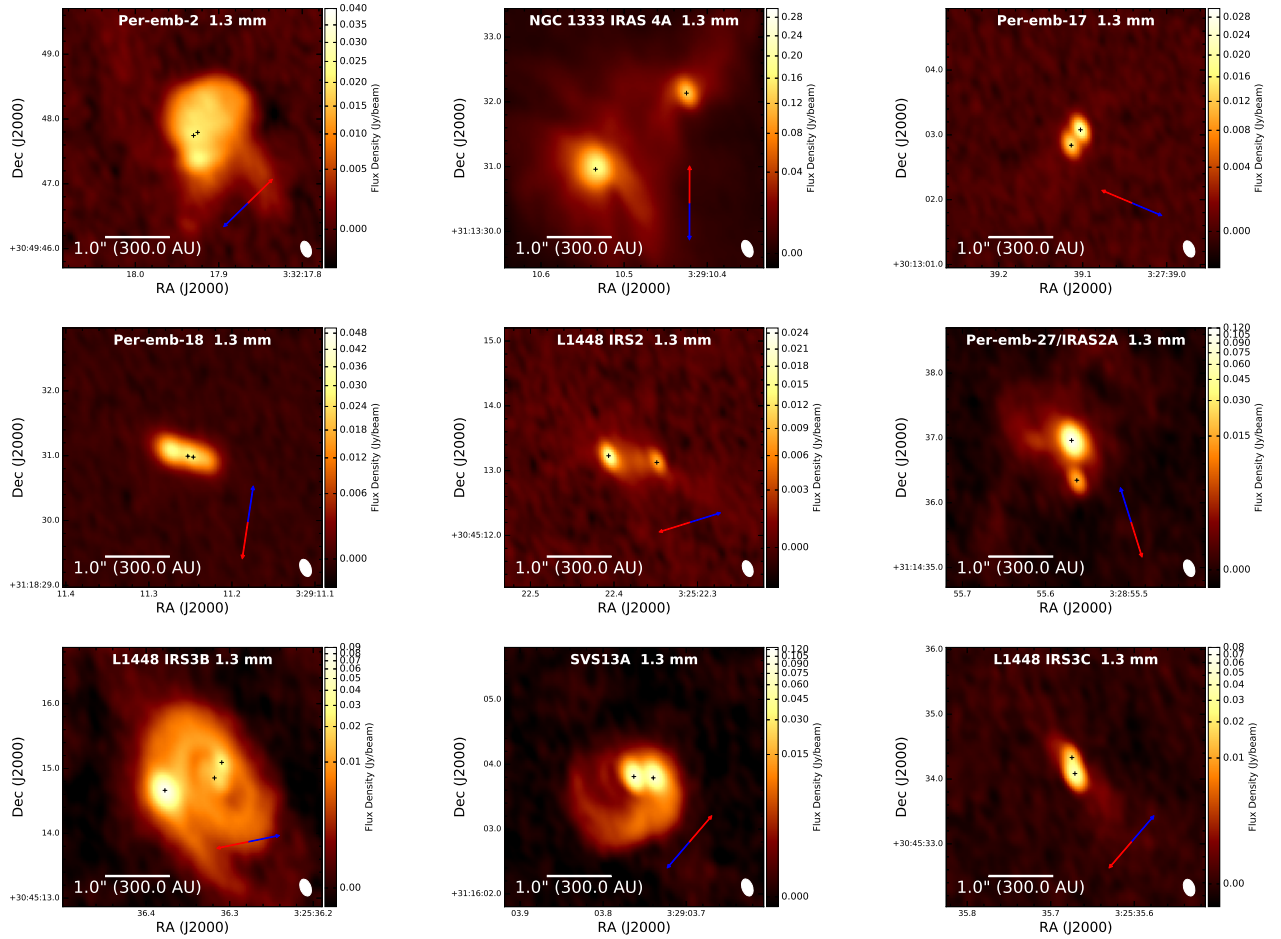


**Figure 1.** ALMA images of Class 0 multiple protostar systems in Perseus at 1.3 mm. The white or black crosses mark the VLA source positions in each image. A 1'' scale bar is also drawn in each panel denoting 300 AU. The beam of each image is drawn in the lower right corner, corresponding to approximately  $0''.27 \times 0''.17$  ( $81 \text{ AU} \times 51 \text{ AU}$ ). The noise level in each image is approximately  $0.14 \text{ mJy beam}^{-1}$ , but this varies somewhat between sources depending on dynamic range limits. The approximate outflow directions (when known) are drawn in the lower right corner with the red and blue arrows directions corresponding to the orientation of the outflow. Note that the outflows apparently originate from the bright continuum peaks, but the arrows are drawn offset for clarity.

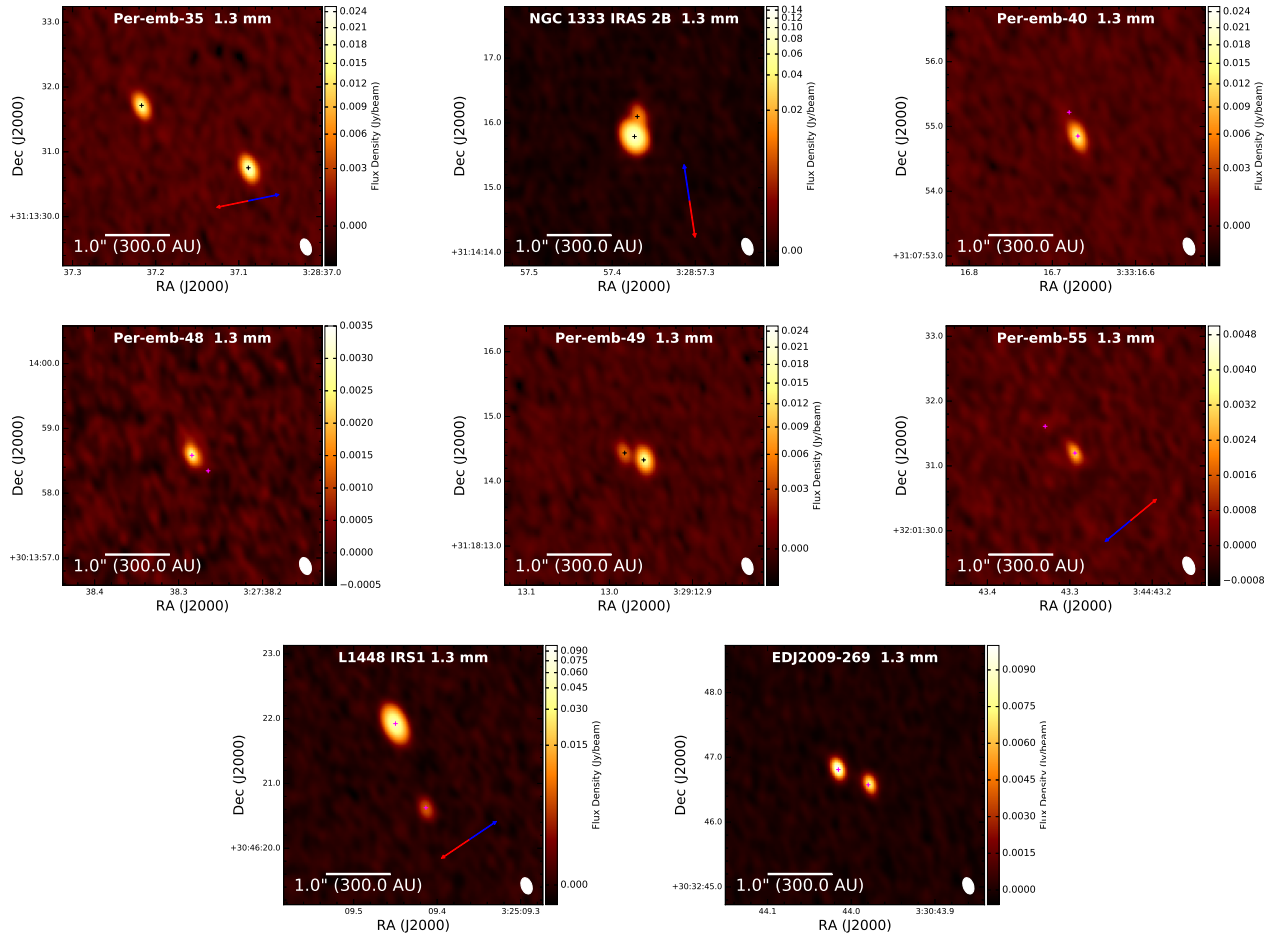


**Figure 2.** Same as Figure 1, except for Class I multiple systems in Perseus.

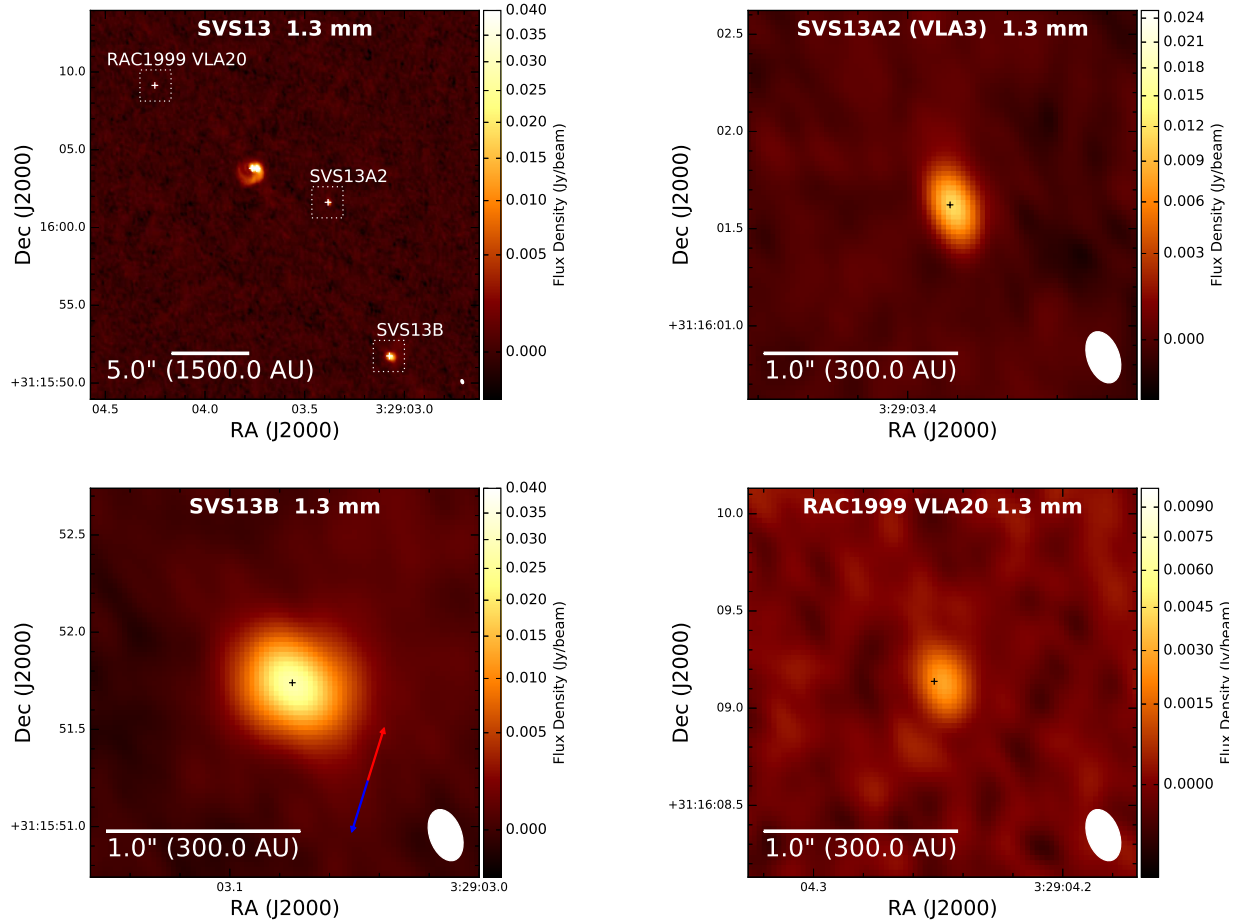


**Figure 3.** ALMA 1.3 mm images of the SVS13 (Per-emb-44) region. A wide view of the region encompassing all the sources within the primary beam is shown in the top left and dashed boxes mark the regions zoomed-in on in the subsequent panels. The northeastern-most source (RAC1999 VLA20) is most likely a background extragalactic source from the VLA imaging results. The two sources south of SVS13A are SVS13A2 (VLA3) and SVS13B. We show the zoom-in on SVS13A2 in the top right panel, the zoom-in on SVS13B in the bottom left panel, and RAC1999 VLA20 in the bottom right panel. SVS13A2 and RAC1999 VLA20 do not appear highly resolved, while SVS13B is clearly resolved with respect to the beam.

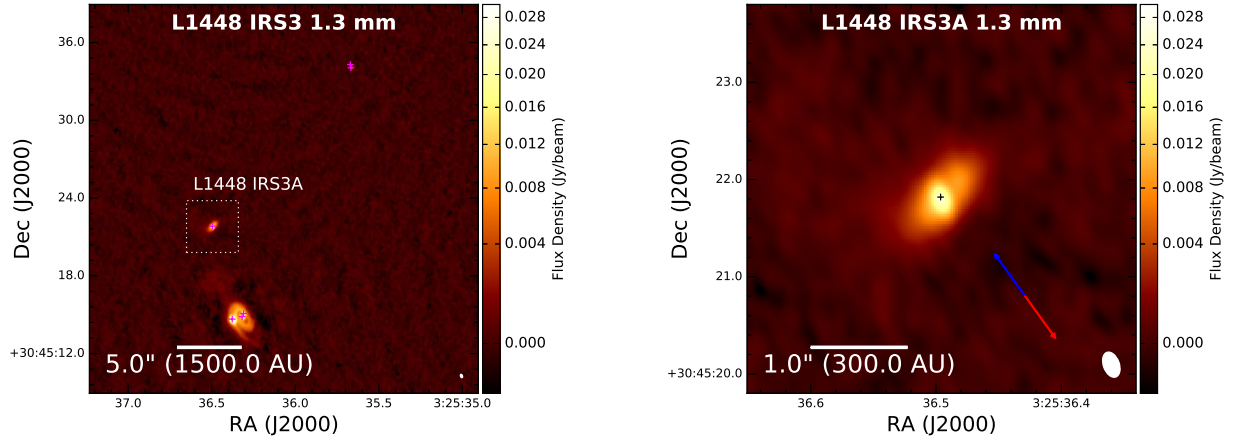


**Figure 4.** ALMA 1.3 mm images of the L1448 IRS3 (Per-emb-33) region encompassing all the sources within the primary beam; the dashed box marks the regions zoomed-in on in the right panel. The observation was centered on L1448 IRS3B largest and brightest source near the bottom of the image. Nonetheless, L1448 IRS3A is detected, source in the middle-left, and L1448 IRS3C (L1448 NW) is marginally detected in this image toward the upper right. L1448 IRS3C was also observed with a separate pointing given its large angular distance from field center. Right: ALMA 1.3 mm zoom-in on L1448 IRS3A showing the resolved disk structure toward this protostar.

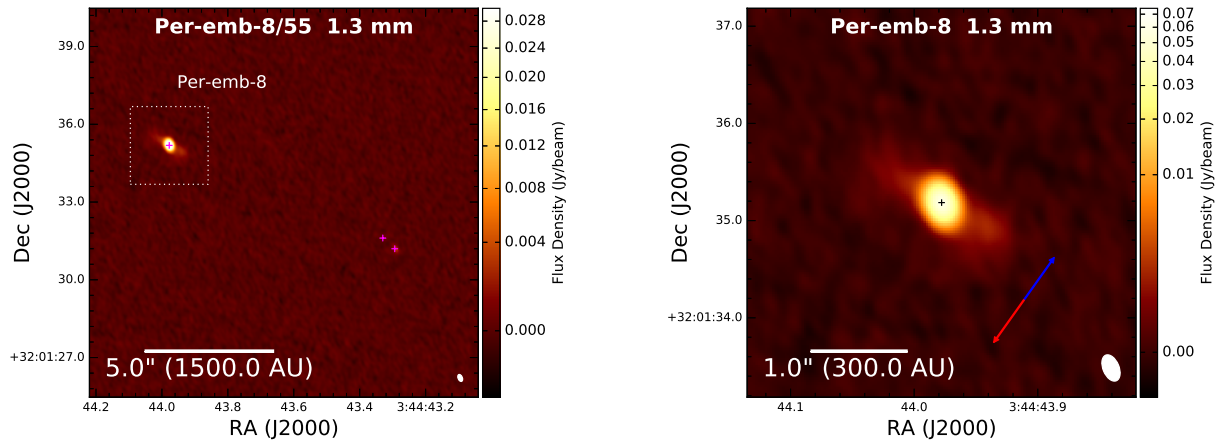


**Figure 5.** ALMA 1.3 mm image of the Per-emb-8/Per-emb-55 region the two sources within the primary beam; the dashed box marks the regions zoomed-in on in the right panel. Per-emb-8 is located in the eastern portion of the image and Per-emb-55 is located in the western portion. Per-emb-8 is clearly resolved and Per-emb-55 is a binary, but only one component is strongly detected. Right: ALMA 1.3 mm image of Per-emb-8, an apparently single source with a surrounding disk. The central region of Per-emb-8 is very prominent with respect to the extended disk.

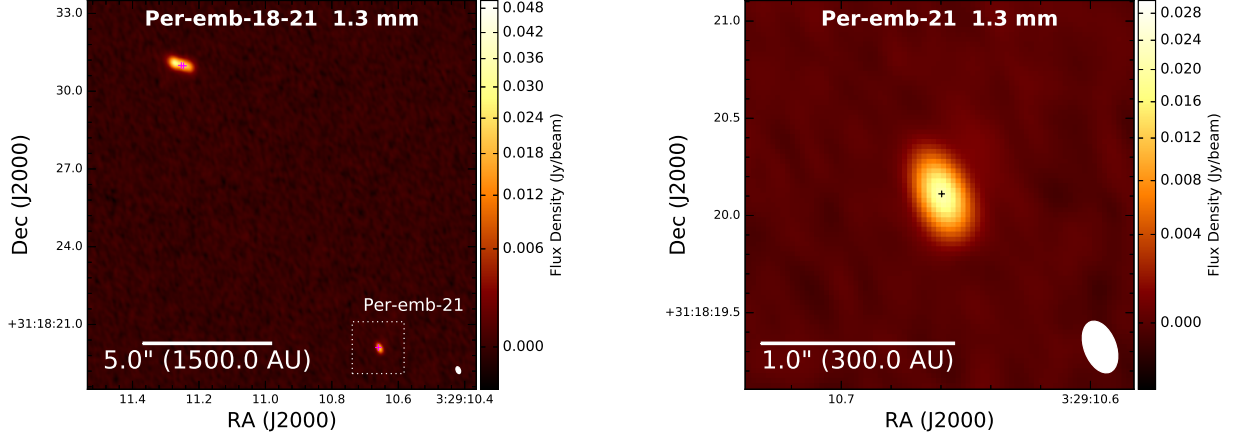


**Figure 6.** ALMA 1.3 mm image of the Per-emb-18/Per-emb-21 region encompassing the two protostars within the primary beam; the dashed box marks the regions zoomed-in on in the right panel. Per-emb-18 is located in the northern portion of the image and Per-emb-21 is located in the southern portion. Right: ALMA 1.3 mm image zooming-in on Per-emb-21, which appears unresolved.

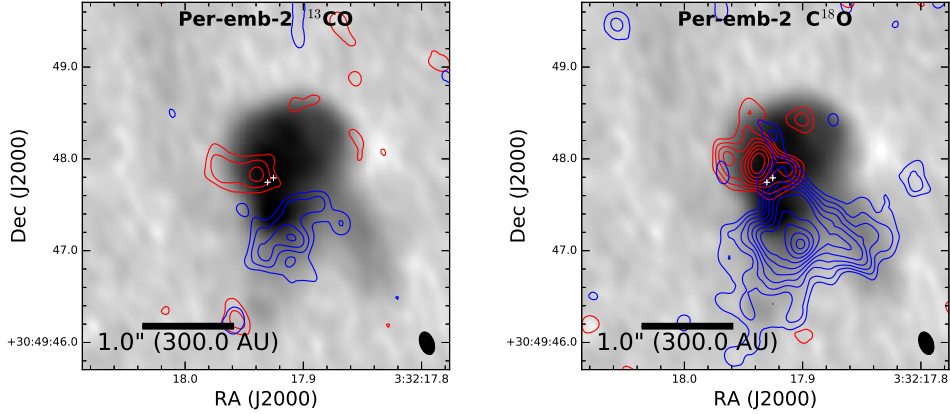


**Figure 7.** Integrated intensity maps of  $^{13}\text{CO}$  (left panel) and  $\text{C}^{18}\text{O}$  (right panel) toward Per-emb-2. The integrated intensity maps are displayed as red and blue contours corresponding to the integrated intensity of line emission red and blue-shifted with respect to the system velocity. The contours are overlaid on the 1.3 mm continuum image. The line emission shows evidence for a velocity gradient consistent with rotation. The red-shifted contours start at  $(4,3)\sigma$  and increase in  $(1,1)\sigma$  increments, and the blue-shifted contours start at  $(3,3)\sigma$  and increase in  $(1,1)\sigma$  increments. The values inside the parentheses in the previous sentence correspond to the  $^{13}\text{CO}$ ,  $\text{C}^{18}\text{O}$ ,  $\text{SO}$ , and  $\text{H}_2\text{CO}$  integrated intensity maps, respectively. The values for  $\sigma_{red}$  and  $\sigma_{blue}$  and velocity ranges over which the line emission was summed can be found in Table 3. The beam in the images is approximately  $0''.36 \times 0''.26$ .

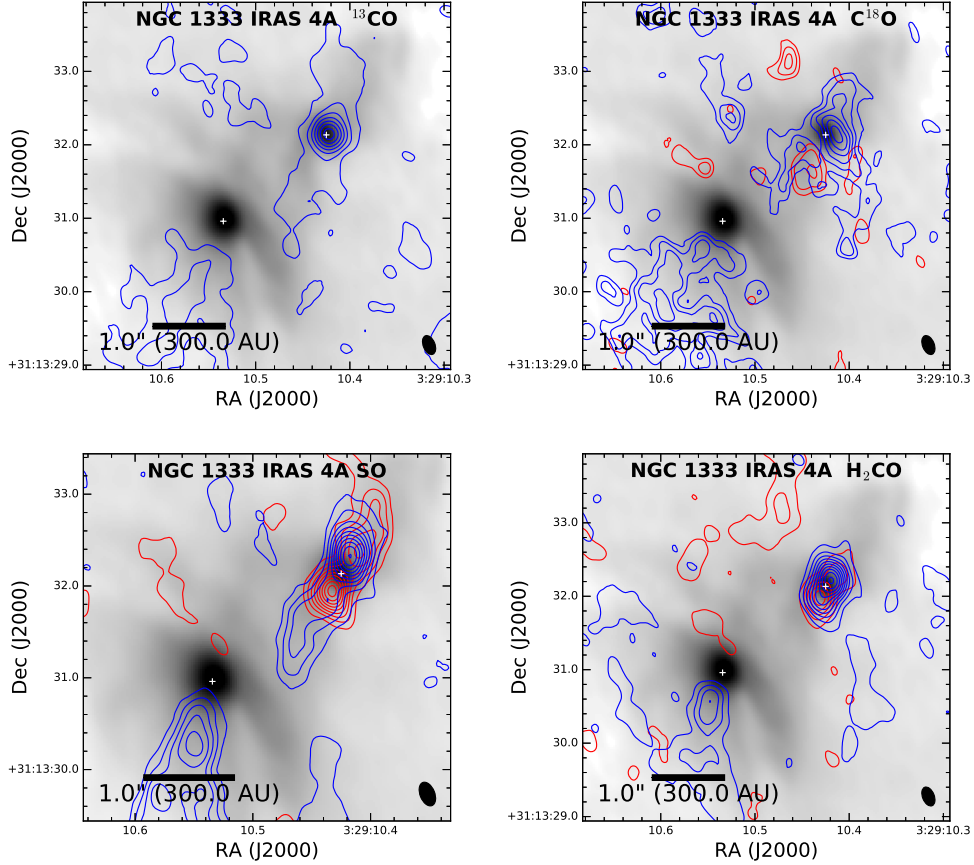


**Figure 8.** Integrated intensity maps of  $^{13}\text{CO}$  (top left panel),  $\text{C}^{18}\text{O}$  (top right panel),  $\text{SO}$  (bottom left panel), and  $\text{H}_2\text{CO}$  (bottom right panel) toward Per-emb-12 (NGC 1333 IRAS4A). The integrated intensity maps are displayed as red and blue contours corresponding to the integrated intensity of line emission red and blue-shifted with respect to the system velocity. The contours are overlaid on the 1.3 mm continuum image. The line emission shows evidence for a velocity gradient consistent with rotation. The red-shifted contours start at  $(3,3,4,3)\sigma$  and increase in  $(3,1,2,3)\sigma$  increments, and the blue-shifted contours start at  $(3,3,4,3)\sigma$  and increase in  $(3,1,2,3)\sigma$  increments. The values inside the parentheses in the previous sentence correspond to the  $^{13}\text{CO}$ ,  $\text{C}^{18}\text{O}$ ,  $\text{SO}$ , and  $\text{H}_2\text{CO}$  integrated intensity maps, respectively. The values for  $\sigma_{red}$  and  $\sigma_{blue}$  and velocity ranges over which the line emission was summed can be found in Table 3. The beam in the images is approximately  $0''.36 \times 0''.26$ .

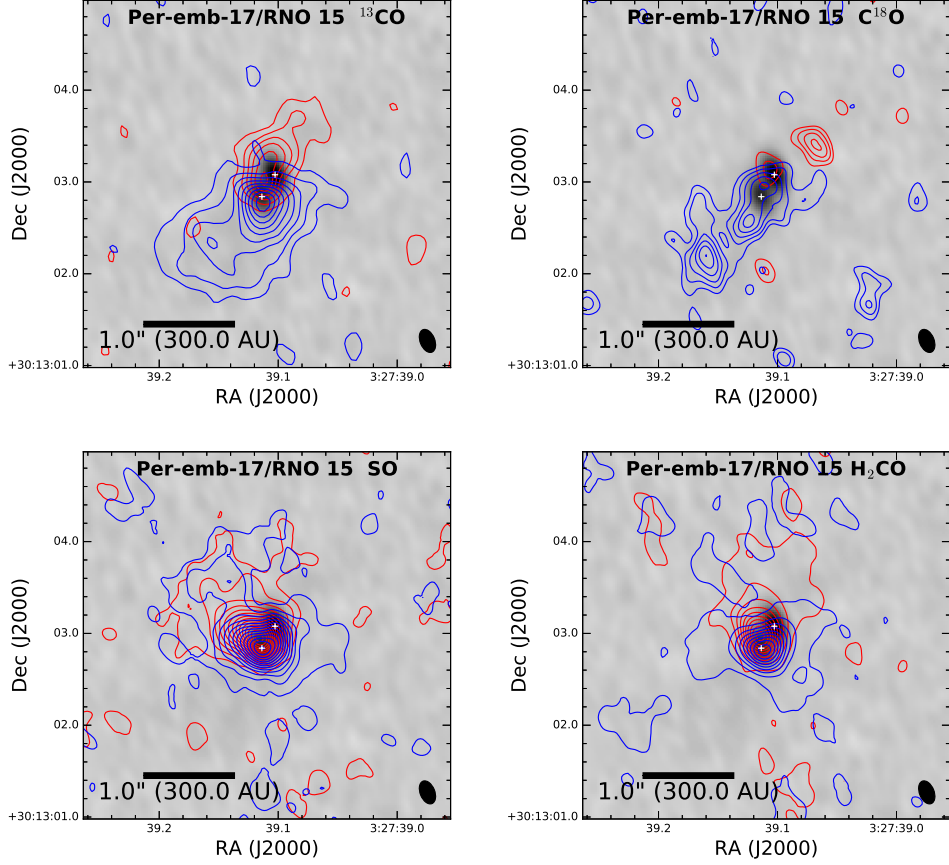


**Figure 9.** Integrated intensity maps of  $^{13}\text{CO}$  (top left panel),  $\text{C}^{18}\text{O}$  (top right panel),  $\text{SO}$  (bottom left panel), and  $\text{H}_2\text{CO}$  (bottom right panel) toward Per-emb-17. The integrated intensity maps are displayed as red and blue contours corresponding to the integrated intensity of line emission red and blue-shifted with respect to the system velocity. The contours are overlaid on the 1.3 mm continuum image. The line emission shows evidence for a velocity gradient consistent with rotation. The red-shifted contours start at  $(3,4,3,3)\sigma$  and increase in  $(2,1,2,3)\sigma$  increments, and the blue-shifted contours start at  $(3,3,3,3)\sigma$  and increase in  $(2,1,2,3)\sigma$  increments. The values inside the parentheses in the previous sentence correspond to the  $^{13}\text{CO}$ ,  $\text{C}^{18}\text{O}$ ,  $\text{SO}$ , and  $\text{H}_2\text{CO}$  integrated intensity maps, respectively. The values for  $\sigma_{red}$  and  $\sigma_{blue}$  and velocity ranges over which the line emission was summed can be found in Table 3. The beam in the images is approximately  $0''.36 \times 0''.26$ .

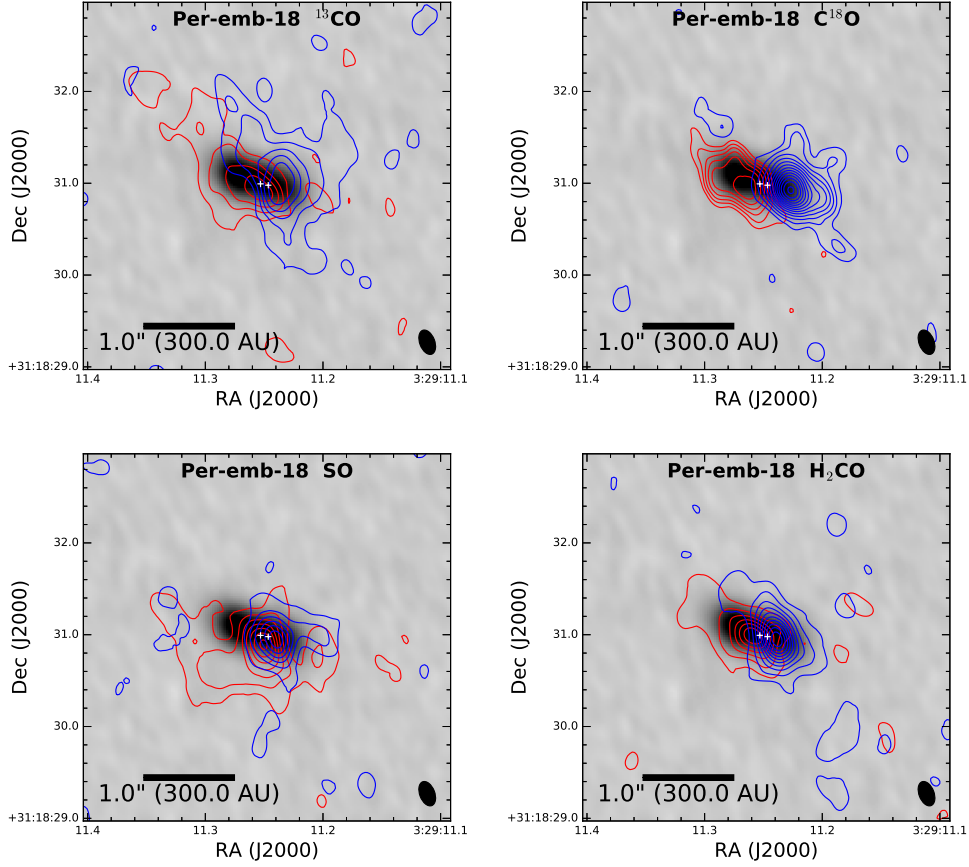


**Figure 10.** Integrated intensity maps of  $^{13}\text{CO}$  (top left panel),  $\text{C}^{18}\text{O}$  (top right panel),  $\text{SO}$  (bottom left panel), and  $\text{H}_2\text{CO}$  (bottom right panel) toward Per-emb-18. The integrated intensity maps are displayed as red and blue contours corresponding to the integrated intensity of line emission red and blue-shifted with respect to the system velocity. The contours are overlaid on the 1.3 mm continuum image. The line emission shows evidence for a velocity gradient consistent with rotation. The red-shifted contours start at  $(3,3,3,3)\sigma$  and increase in  $(2,1,2,2)\sigma$  increments, and the blue-shifted contours start at  $(3,4,3,3)\sigma$  and increase in  $(2,1,2,2)\sigma$  increments. The values inside the parentheses in the previous sentence correspond to the  $^{13}\text{CO}$ ,  $\text{C}^{18}\text{O}$ ,  $\text{SO}$ , and  $\text{H}_2\text{CO}$  integrated intensity maps, respectively. The values for  $\sigma_{red}$  and  $\sigma_{blue}$  and velocity ranges over which the line emission was summed can be found in Table 3. The beam in the images is approximately  $0''.36 \times 0''.26$ .

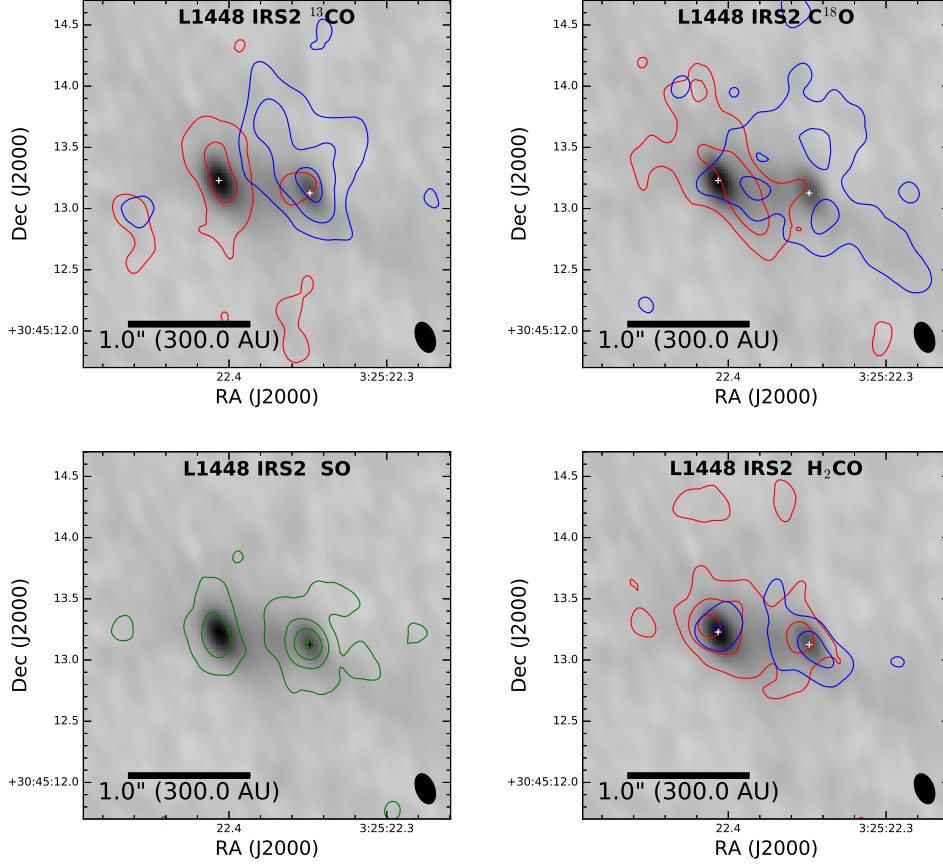


**Figure 11.** Integrated intensity maps of  $^{13}\text{CO}$  (top left panel),  $\text{C}^{18}\text{O}$  (top right panel),  $\text{SO}$  (bottom left panel), and  $\text{H}_2\text{CO}$  (bottom right panel) toward Per-emb-22 (L1448 IRS2). The integrated intensity maps are displayed as red and blue contours corresponding to the integrated intensity of line emission red and blue-shifted with respect to the system velocity. The green contours for the  $\text{SO}$  emission correspond to emission integrated across the entire line because there was not a clear velocity gradient in this molecule due to low S/N. The contours are overlaid on the 1.3 mm continuum image. The line emission shows evidence for a velocity gradient consistent with rotation. The red-shifted contours start at  $(3,3,3,4)\sigma$  and increase in  $(3,3,3,2)\sigma$  increments, and the blue-shifted contours start at  $(3,3,3,4)\sigma$  and increase in  $(3,3,3,2)\sigma$  increments. The values inside the parentheses in the previous sentence correspond to the  $^{13}\text{CO}$ ,  $\text{C}^{18}\text{O}$ ,  $\text{SO}$ , and  $\text{H}_2\text{CO}$  integrated intensity maps, respectively. The values for  $\sigma_{red}$  and  $\sigma_{blue}$  and velocity ranges over which the line emission was summed can be found in Table 3. The beam in the images is approximately  $0''.36 \times 0''.26$ .

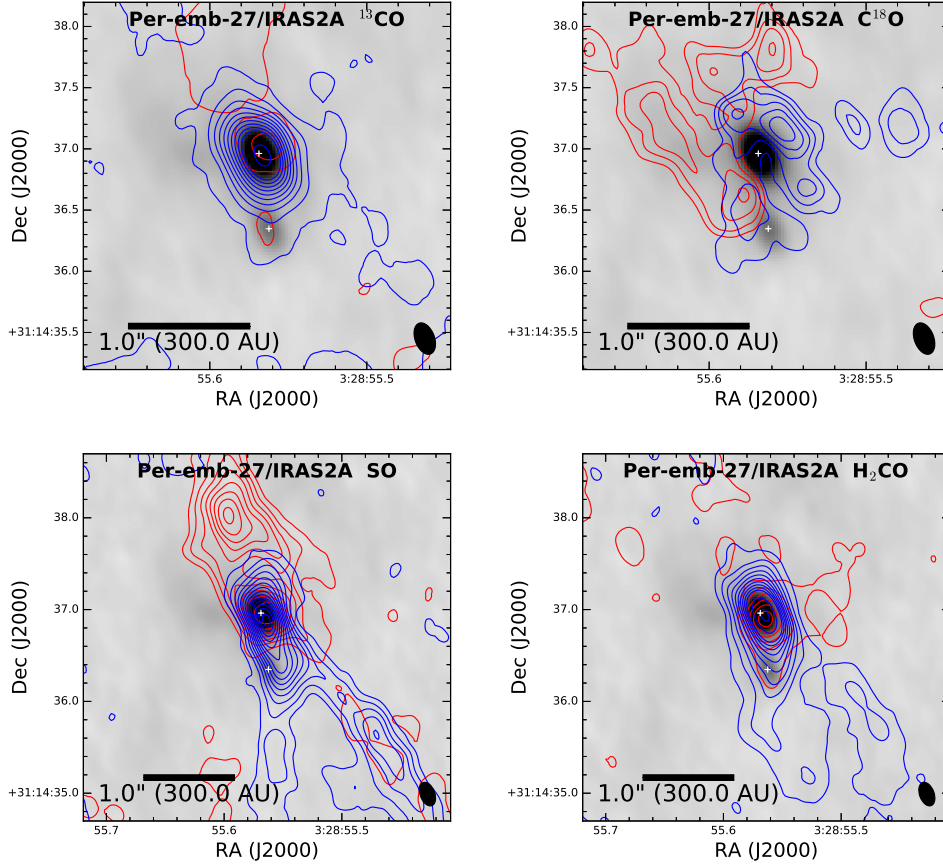


**Figure 12.** Integrated intensity maps of  $^{13}\text{CO}$  (top left panel),  $\text{C}^{18}\text{O}$  (top right panel),  $\text{SO}$  (bottom left panel), and  $\text{H}_2\text{CO}$  (bottom right panel) toward Per-emb-27 (NGC 1333 IRAS2A). The integrated intensity maps are displayed as red and blue contours corresponding to the integrated intensity of line emission red and blue-shifted with respect to the system velocity. The contours are overlaid on the 1.3 mm continuum image. The line emission shows evidence for a velocity gradient consistent with rotation. The red-shifted contours start at  $(3,3,3,3)\sigma$  and increase in  $(3,1,2,3)\sigma$  increments, and the blue-shifted contours start at  $(3,3,3,3)\sigma$  and increase in  $(3,1,2,3)\sigma$  increments. The values inside the parentheses in the previous sentence correspond to the  $^{13}\text{CO}$ ,  $\text{C}^{18}\text{O}$ ,  $\text{SO}$ , and  $\text{H}_2\text{CO}$  integrated intensity maps, respectively. The values for  $\sigma_{red}$  and  $\sigma_{blue}$  and velocity ranges over which the line emission was summed can be found in Table 3. The beam in the images is approximately  $0''.36 \times 0''.26$ .

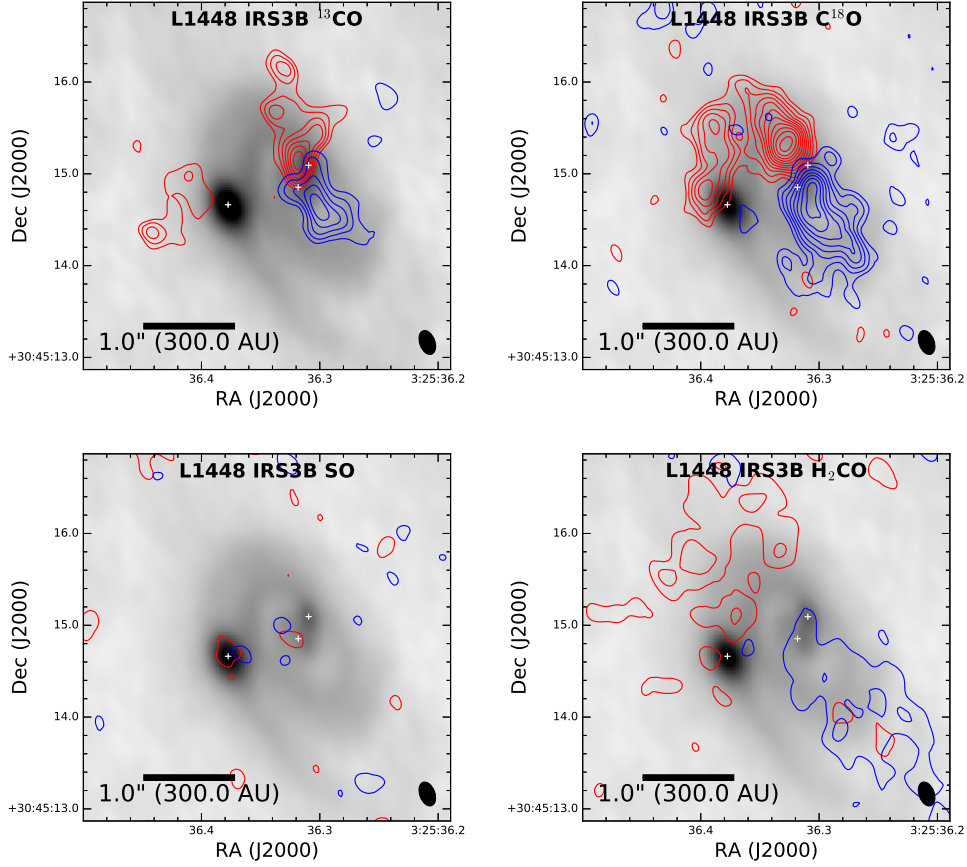


**Figure 13.** Integrated intensity maps of  $^{13}\text{CO}$  (top left panel),  $\text{C}^{18}\text{O}$  (top right panel),  $\text{SO}$  (bottom left panel), and  $\text{H}_2\text{CO}$  (bottom right panel) toward Per-emb-33 (L1448 IRS3B). The integrated intensity maps are displayed as red and blue contours corresponding to the integrated intensity of line emission red and blue-shifted with respect to the system velocity. The contours are overlaid on the 1.3 mm continuum image. The line emission shows evidence for a velocity gradient consistent with rotation. The red-shifted contours start at  $(4,4,3,3)\sigma$  and increase in  $(1,1,2,2)\sigma$  increments, and the blue-shifted contours start at  $(4,4,3,3)\sigma$  and increase in  $(1,1,2,2)\sigma$  increments. The values inside the parentheses in the previous sentence correspond to the  $^{13}\text{CO}$ ,  $\text{C}^{18}\text{O}$ ,  $\text{SO}$ , and  $\text{H}_2\text{CO}$  integrated intensity maps, respectively. The values for  $\sigma_{red}$  and  $\sigma_{blue}$  and velocity ranges over which the line emission was summed can be found in Table 3. The beam in the images is approximately  $0''.36 \times 0''.26$ .

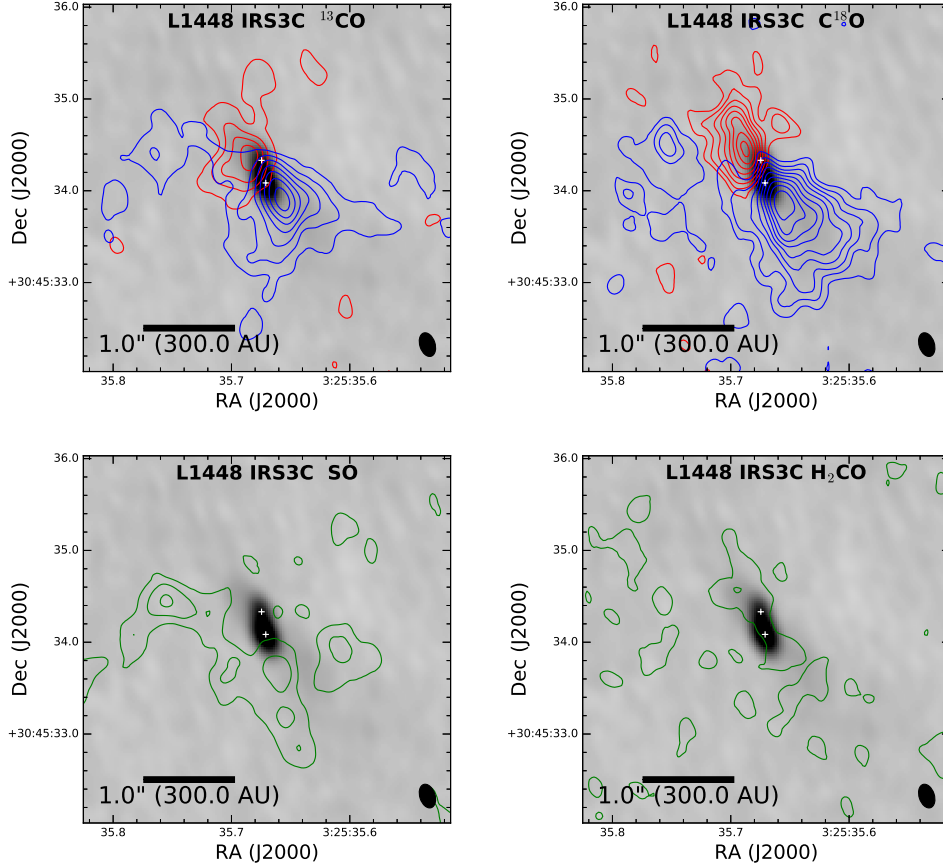


**Figure 14.** Integrated intensity maps of  $^{13}\text{CO}$  (top left panel),  $\text{C}^{18}\text{O}$  (top right panel), SO (bottom left panel), and  $\text{H}_2\text{CO}$  (bottom right panel) toward L1448 IRS3C (L1448 NW). The integrated intensity maps are displayed as red and blue contours corresponding to the integrated intensity of line emission red and blue-shifted with respect to the system velocity. The contours are overlaid on the 1.3 mm continuum image. The line emission shows evidence for a velocity gradient consistent with rotation. The red-shifted contours start at  $(3,4)\sigma$  and increase in  $(2,1)\sigma$  increments, and the blue-shifted contours start at  $(3,3)\sigma$  and increase in  $(2,1)\sigma$  increments. The contours for SO and  $\text{H}_2\text{CO}$  start  $(3,3)\sigma$  and increase in  $(2,3)\sigma$ , respectively for a single interval. The values for  $\sigma$ ,  $\sigma_{red}$  and  $\sigma_{blue}$  and velocity ranges over which the line emission was summed can be found in Table 3. The beam in the images is approximately  $0''.36 \times 0''.26$ .

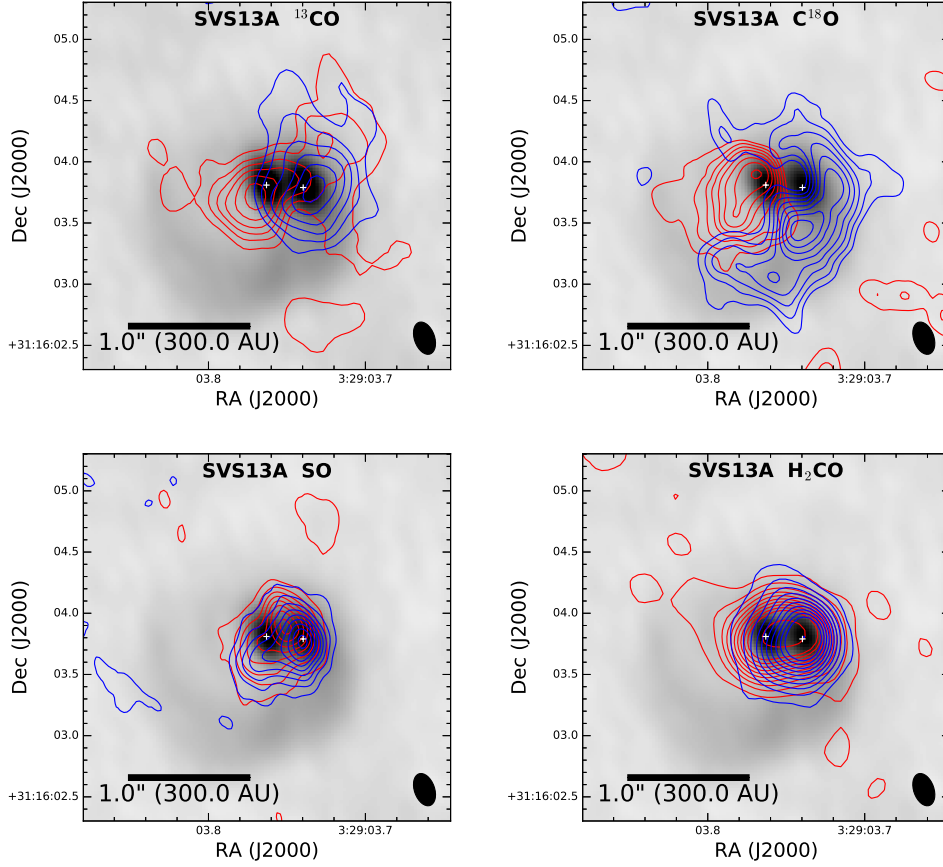


**Figure 15.** Integrated intensity maps of  $^{13}\text{CO}$  (top left panel),  $\text{C}^{18}\text{O}$  (top right panel),  $\text{SO}$  (bottom left panel), and  $\text{H}_2\text{CO}$  (bottom right panel) toward Per-emb-44 (SVS13A). The integrated intensity maps are displayed as red and blue contours corresponding to the integrated intensity of line emission red and blue-shifted with respect to the system velocity. The contours are overlaid on the 1.3 mm continuum image. The line emission shows evidence for a velocity gradient consistent with rotation. The red-shifted contours start at  $(4,3,5,5)\sigma$  and increase in  $(2,1,5,5)\sigma$  increments, and the blue-shifted contours start at  $(4,3,5,5)\sigma$  and increase in  $(2,1,5,5)\sigma$  increments. The values inside the parentheses in the previous sentence correspond to the  $^{13}\text{CO}$ ,  $\text{C}^{18}\text{O}$ ,  $\text{SO}$ , and  $\text{H}_2\text{CO}$  integrated intensity maps, respectively. The values for  $\sigma_{red}$  and  $\sigma_{blue}$  and velocity ranges over which the line emission was summed can be found in Table 3. The beam in the images is approximately  $0''.36 \times 0''.26$ .

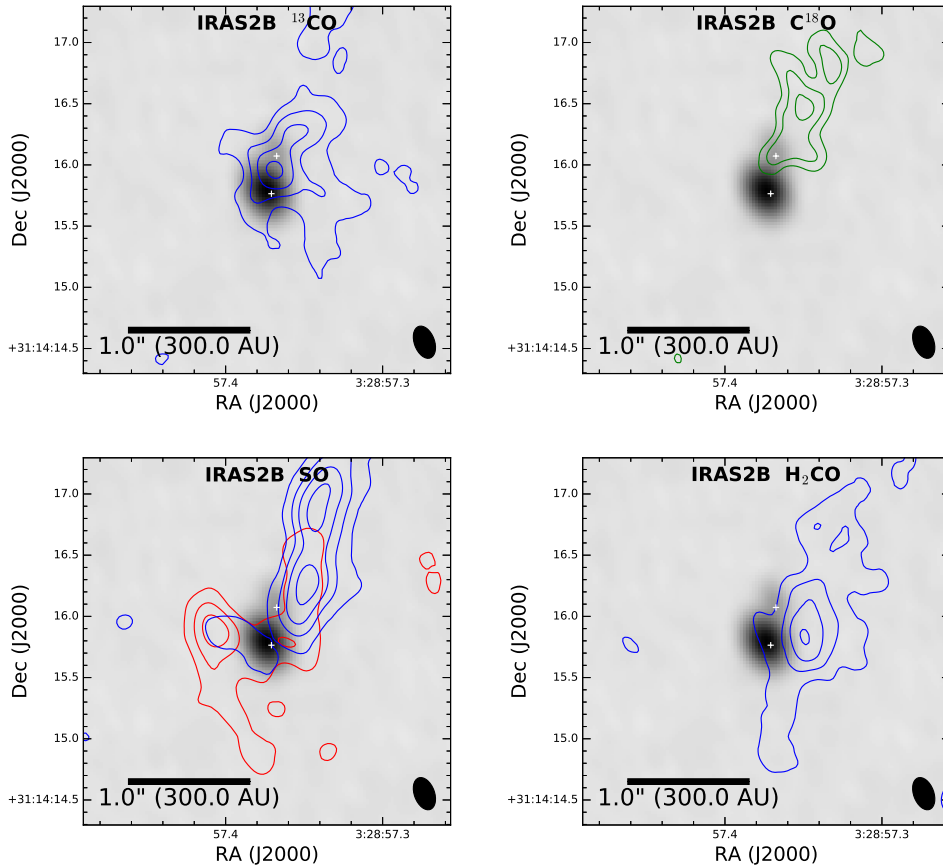


**Figure 16.** Integrated intensity maps of  $^{13}\text{CO}$  (top left panel),  $\text{C}^{18}\text{O}$  (top right panel),  $\text{SO}$  (bottom left panel), and  $\text{H}_2\text{CO}$  (bottom right panel) toward Per-emb-36 (NGC 1333 IRAS2B). The integrated intensity maps are displayed as red and blue contours corresponding to the integrated intensity of line emission red and blue-shifted with respect to the system velocity. The contours are overlaid on the 1.3 mm continuum image. The line emission shows evidence for a velocity gradient consistent with rotation. The red-shifted contours start at  $(4,3)\sigma$  and increase in  $(2,3)\sigma$  increments for  $^{13}\text{CO}$  and  $\text{SO}$ , respectively, and the blue-shifted contours start at  $(3,3,3)\sigma$  and increase in  $(2,3,2)\sigma$  increments for  $^{13}\text{CO}$ ,  $\text{SO}$ , and  $\text{H}_2\text{CO}$ , respectively. The line-center contours for  $\text{C}^{18}\text{O}$  start at  $3\sigma$  and increase by  $1\sigma$  increments. The values for  $\sigma_{red}$  and  $\sigma_{blue}$  and velocity ranges over which the line emission was summed can be found in Table 3. The beam in the images is approximately  $0''.36 \times 0''.26$ .

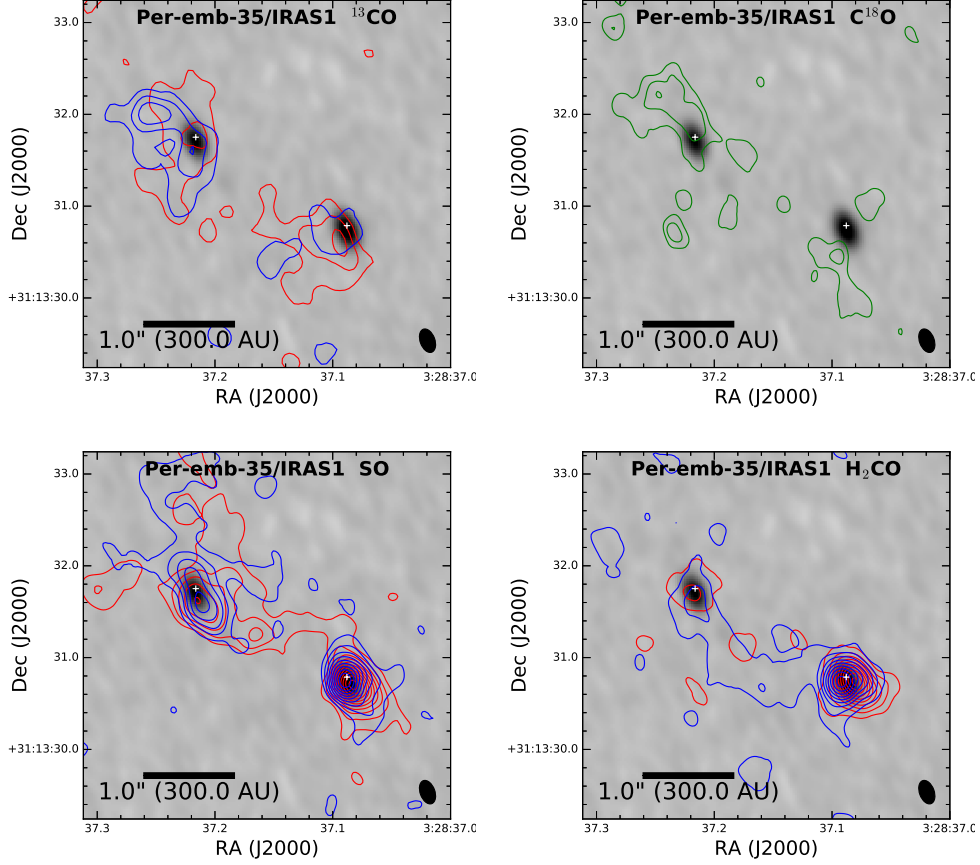


**Figure 17.** Integrated intensity maps of  $^{13}\text{CO}$  (top left panel),  $\text{C}^{18}\text{O}$  (top right panel), SO (bottom left panel), and  $\text{H}_2\text{CO}$  (bottom right panel) toward Per-emb-35 (NGC 1333 IRAS1). The integrated intensity maps are displayed as red and blue contours corresponding to the integrated intensity of line emission red and blue-shifted with respect to the system velocity. The contours are overlaid on the 1.3 mm continuum image. The line emission shows evidence for a velocity gradient consistent with rotation. The red-shifted contours start at  $(3,3,3,3)\sigma$  and increase in  $(2,1,2,2)\sigma$  increments and the blue-shifted contours start at  $(3,3,3,3)\sigma$  and increase in  $(2,1,2,2)\sigma$  increments, respectively. The values inside the parentheses in the previous sentence correspond to the  $^{13}\text{CO}$ ,  $\text{C}^{18}\text{O}$ , SO, and  $\text{H}_2\text{CO}$  integrated intensity maps, respectively. The values for  $\sigma_{red}$  and  $\sigma_{blue}$  and velocity ranges over which the line emission was summed can be found in Table 3. The beam in the images is approximately  $0''.36 \times 0''.26$ .

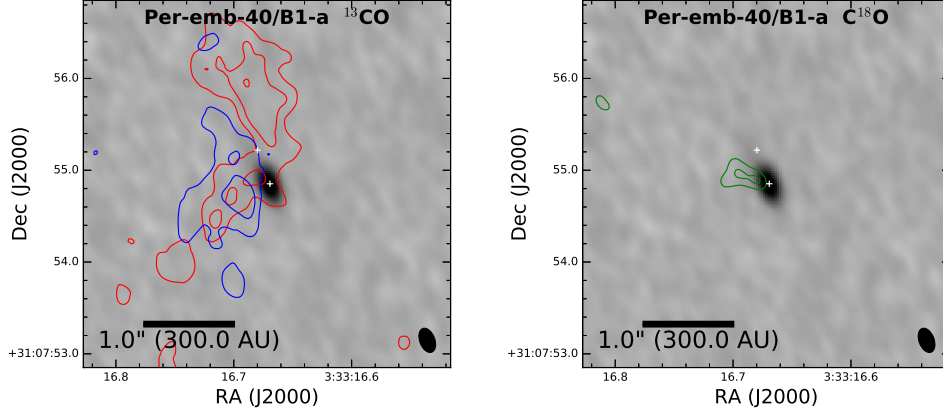


**Figure 18.** Integrated intensity maps of  $^{13}\text{CO}$  (top left panel),  $\text{C}^{18}\text{O}$  (top right panel),  $\text{SO}$  (bottom left panel), and  $\text{H}_2\text{CO}$  (bottom right panel) toward Per-emb-40 (B1-a). The integrated intensity maps are displayed as red and blue contours corresponding to the integrated intensity of line emission red and blue-shifted with respect to the system velocity. The contours are overlaid on the 1.3 mm continuum image. The line emission shows evidence for a velocity gradient consistent with rotation. The red-shifted contours start at  $3\sigma$  and increase in  $2\sigma$  increments, and the blue-shifted contours start at  $3\sigma$  and increase in  $2\sigma$  increments. For  $\text{C}^{18}\text{O}$  only the line center velocities are plotted, starting at  $4\sigma$  and increasing by  $1\sigma$  intervals. The values for  $\sigma_{red}$  and  $\sigma_{blue}$  and velocity ranges over which the line emission was summed can be found in Table 3. The beam in the images is approximately  $0''.36 \times 0''.26$ .

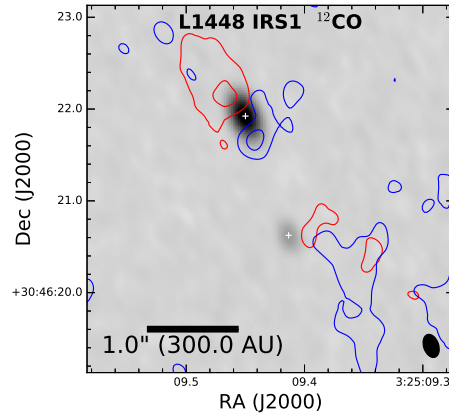


**Figure 19.** Integrated intensity maps of  $^{12}\text{CO}$  toward L1448 IRS1. The integrated intensity maps are displayed as red and blue contours corresponding to the integrated intensity of line emission red and blue-shifted with respect to the system velocity. The contours are overlaid on the 1.3 mm continuum image. The line emission shows evidence for a velocity gradient consistent with rotation. The red-shifted contours start at  $3\sigma$  and increase in  $3\sigma$  increments, and the blue-shifted contours start at  $3\sigma$  and increase in  $3\sigma$  increments. The values for  $\sigma_{red}$  and  $\sigma_{blue}$  and velocity ranges over which the line emission was summed can be found in Table 3. The beam in the images is approximately  $0''.36 \times 0''.26$ .

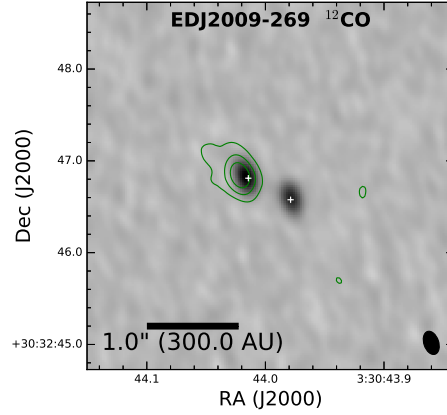


**Figure 20.** Integrated intensity maps of  $^{12}\text{CO}$  toward EDJ2009-269. The integrated intensity maps are displayed as red and blue contours corresponding to the integrated intensity of line emission red and blue-shifted with respect to the system velocity. The contours are overlaid on the 1.3 mm continuum image. The line emission shows evidence for a velocity gradient consistent with rotation. The integrated intensity contours start at  $3\sigma$  and increase in  $3\sigma$  increments. The values for  $\sigma$  and the velocity range over which the line emission was summed can be found in Table 3. The beam in the images is approximately  $0''.36 \times 0''.26$ .

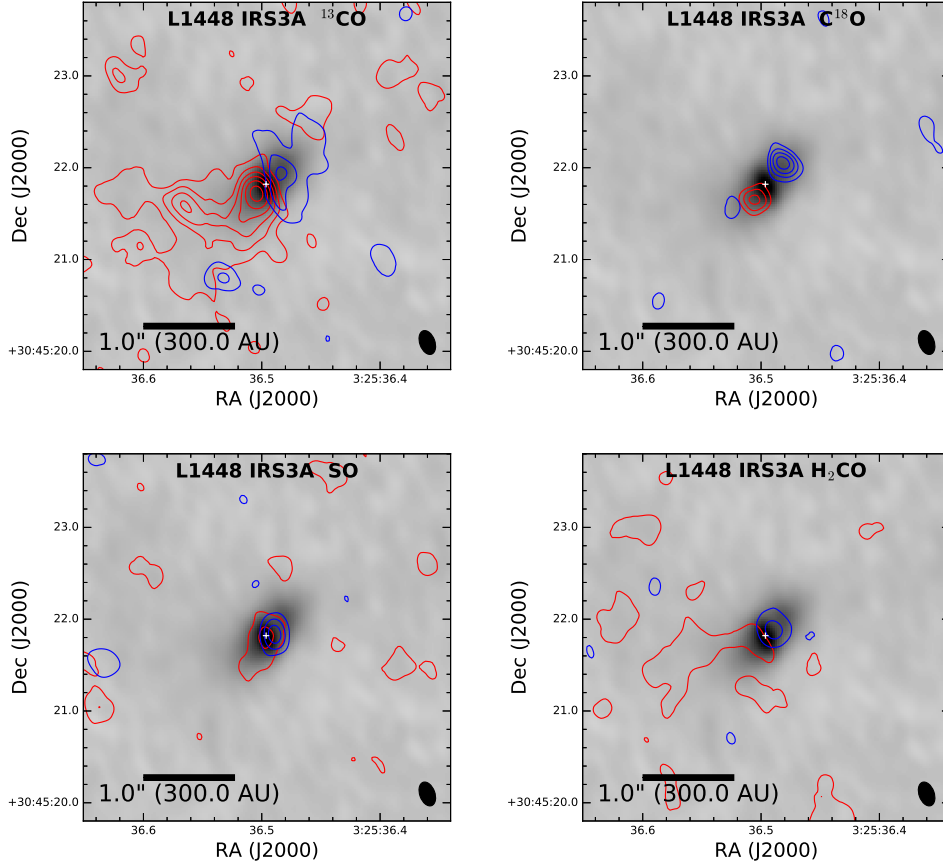


**Figure 21.** Integrated intensity maps of  $^{13}\text{CO}$  (top left panel),  $\text{C}^{18}\text{O}$  (top right panel),  $\text{SO}$  (bottom left panel), and  $\text{H}_2\text{CO}$  (bottom right panel) toward L1448 IRS3A. The integrated intensity maps are displayed as red and blue contours corresponding to the integrated intensity of line emission red and blue-shifted with respect to the system velocity. The contours are overlaid on the 1.3 mm continuum image. The line emission shows evidence for a velocity gradient consistent with rotation. The red-shifted contours start at  $(3,4,3,3)\sigma$  and increase in  $(2,1,2,3)\sigma$  increments, and the blue-shifted contours start at  $(3,3,3,3)\sigma$  and increase in  $(2,1,2,3)\sigma$  increments. The values inside the parentheses in the previous sentence correspond to the  $^{13}\text{CO}$ ,  $\text{C}^{18}\text{O}$ ,  $\text{SO}$ , and  $\text{H}_2\text{CO}$  integrated intensity maps, respectively. The values for  $\sigma_{red}$  and  $\sigma_{blue}$  and velocity ranges over which the line emission was summed can be found in Table 3. The beam in the images is approximately  $0''.36 \times 0''.26$ .

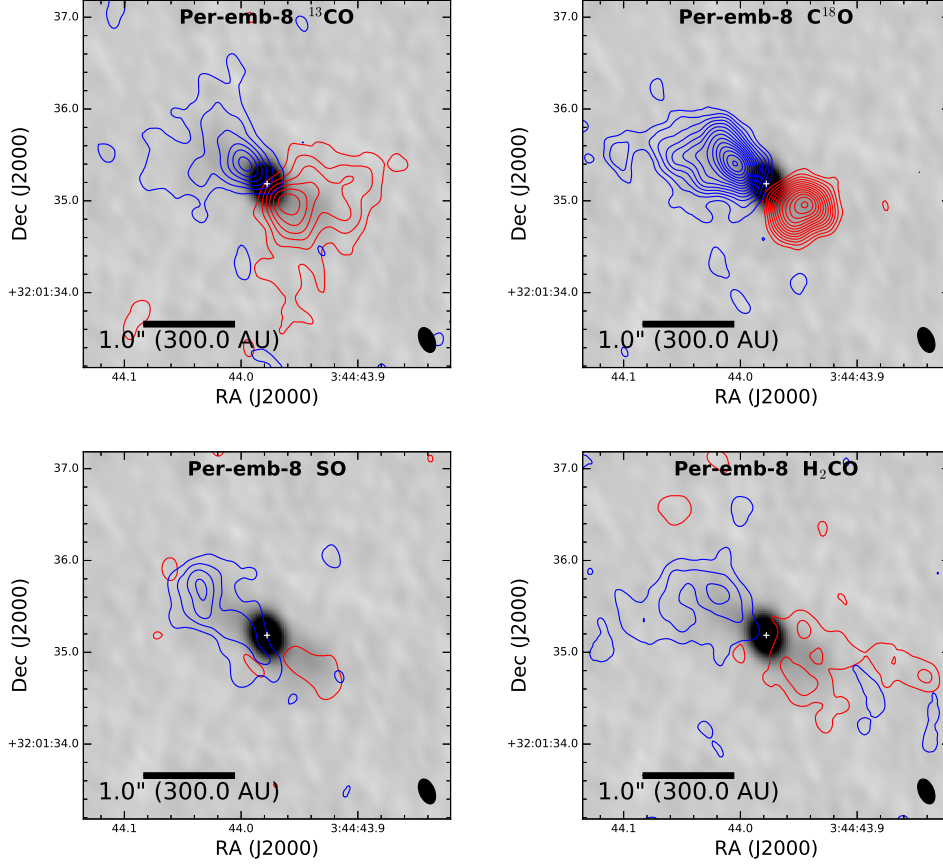


**Figure 22.** Integrated intensity maps of  $^{13}\text{CO}$  (top left panel),  $\text{C}^{18}\text{O}$  (top right panel),  $\text{SO}$  (bottom left panel), and  $\text{H}_2\text{CO}$  (bottom right panel) toward Per-emb-8. The integrated intensity maps are displayed as red and blue contours corresponding to the integrated intensity of line emission red and blue-shifted with respect to the system velocity. The contours are overlaid on the 1.3 mm continuum image. The line emission shows evidence for a velocity gradient consistent with rotation. The red-shifted contours start at  $(3,4,3,3)\sigma$  and increase in  $(2,1,2,2)\sigma$  increments, and the blue-shifted contours start at  $(3,3,3,3)\sigma$  and increase in  $(2,1,2,2)\sigma$  increments. The values inside the parentheses in the previous sentence correspond to the  $^{13}\text{CO}$ ,  $\text{C}^{18}\text{O}$ ,  $\text{SO}$ , and  $\text{H}_2\text{CO}$  integrated intensity maps, respectively. The values for  $\sigma_{red}$  and  $\sigma_{blue}$  and velocity ranges over which the line emission was summed can be found in Table 3. The beam in the images is approximately  $0''.36 \times 0''.26$ .

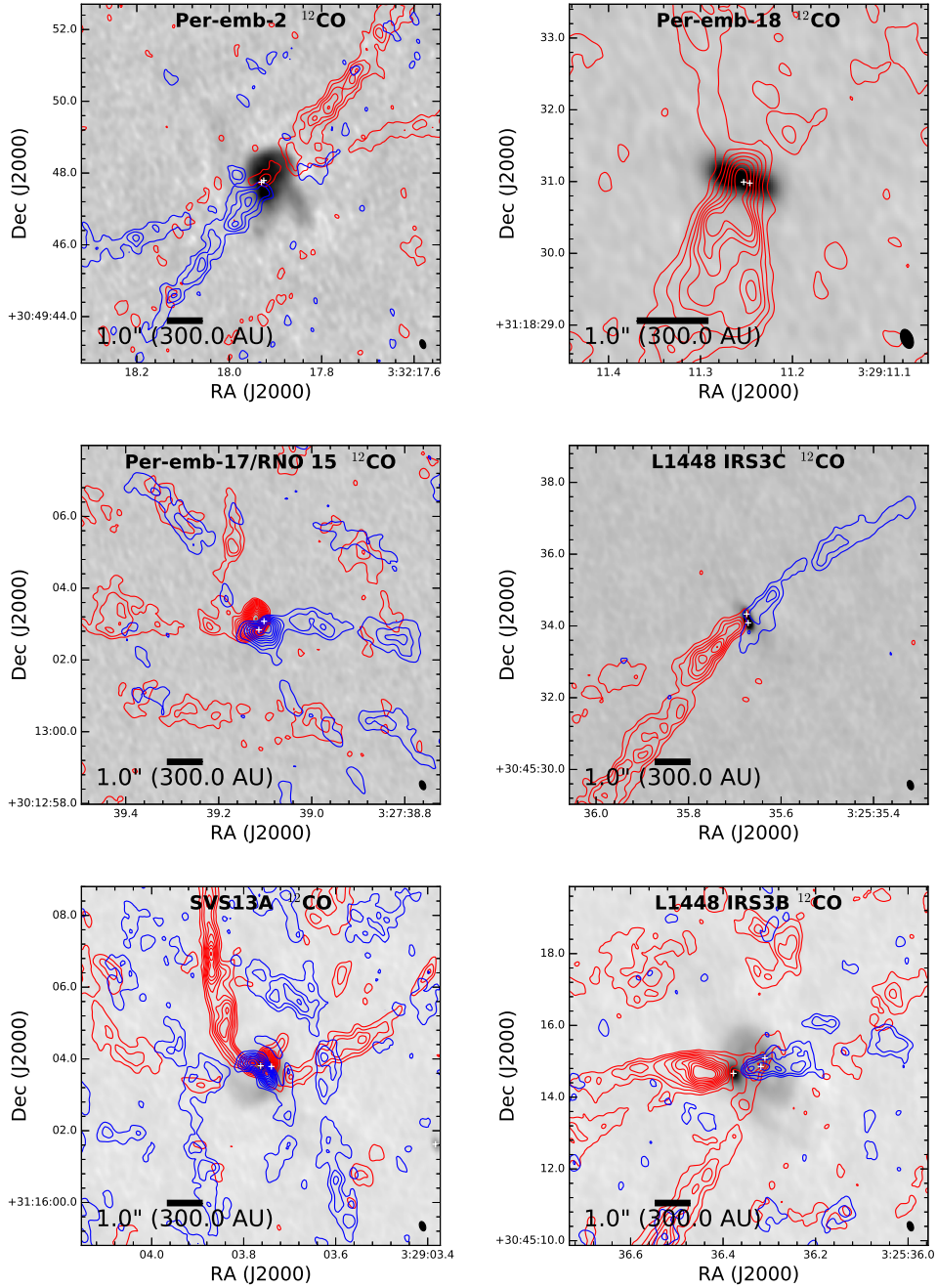


**Figure 23.** ALMA  $^{12}\text{CO}$  integrated intensity maps toward all protostars where  $^{12}\text{CO}$  appears to trace outflowing gas from the protostellar system. The integrated intensity maps are displayed as red and blue contours corresponding to the integrated intensity of line emission red and blue-shifted with respect to the system velocity. The contours are overlaid on the 1.3 mm continuum image. The line emission shows evidence for a velocity gradient consistent with rotation. The red-shifted contours start at  $X\sigma$  and increase in  $X\sigma$  increments, and the blue-shifted contours start at  $X\sigma$  and increase in  $X\sigma$  increments. The values for  $\sigma_{red}$  and  $\sigma_{blue}$  and velocity ranges over which the line emission was summed can be found in Table 3. The beam in the images is approximately  $0''.36 \times 0''.26$ .

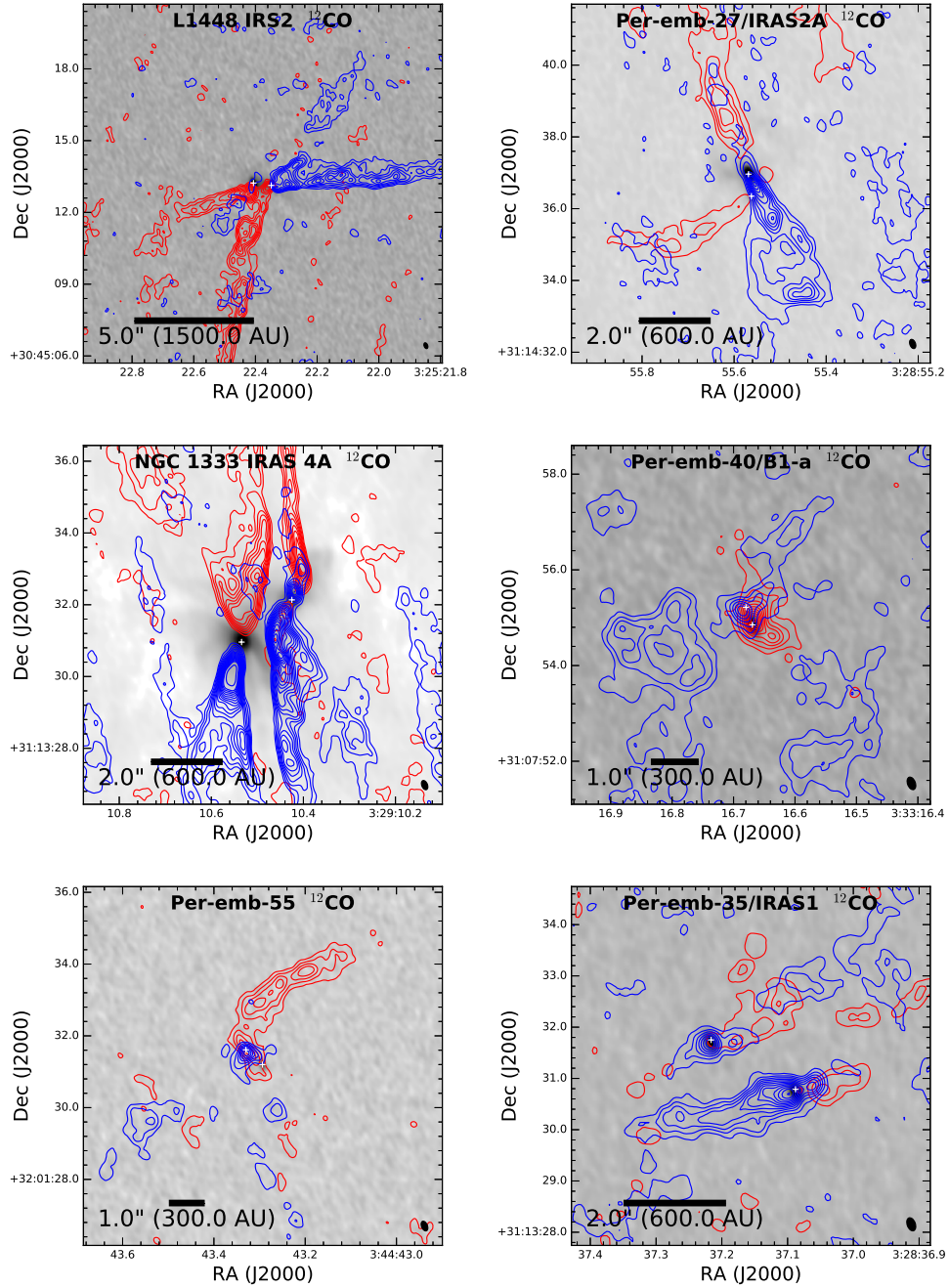


Figure 24. Same as Figure 23.

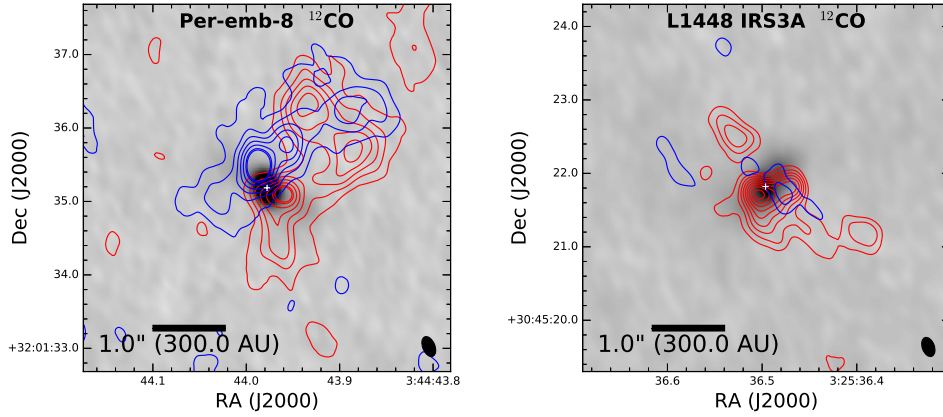


Figure 25. Same as Figure 23.

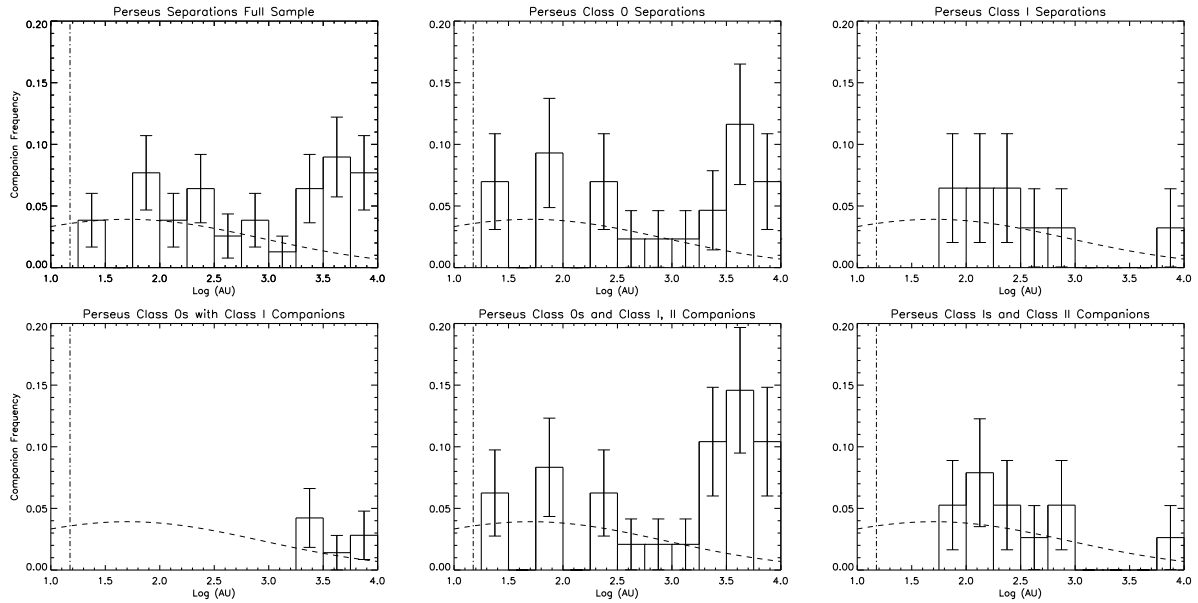


Figure 26. Histograms of companion frequency versus separation for multiple sources in Perseus; this is an updated version of the plot shown in Tobin et al. (2016b), but with the average distance to Perseus revised to 300 pc. The top left panel shows the distribution for all sources in the sample; the top middle and top right panels break the distribution into sources that are only comprised of Class 0 protostars and Class I protostars, respectively. The bottom left panel shows only the multiple systems comprised of Class 0 and I sources, the bottom middle shows the separation distribution of all systems with a Class 0 primary source and the bottom left panel shows the same, but with a Class I primary. The systems comprised of a Class 0 and Class I protostar are not included in the Class I plot in the bottom right. Note the apparent bi-modal distribution for the full sample and Class 0 samples and the apparent deficit of wide companions for the Class I systems. In all plots, the dashed curve is the Gaussian fit to the field star separation distribution from Raghavan et al. (2010) and the vertical dot-dashed line corresponds to the approximate resolution limit of 20 AU.

Table 1. Source List and Gaussian Fitting Results

Source	RA (J2000)	Decl. (J2000)	Int. Flux (mJy)	Peak Flux (mJy beam <sup>-1</sup> )	$\theta_{maj} \times \theta_{min}$ (" × ")	PA (°)	Deconv. $\theta_{maj}$ (arcsec)	Deconv. $\theta_{min}$ (arcsec)	Deconv. PA (°)	Extended Flux (mJy)	Spectral Index
Per-emb-12-A	3:29:10.53	31:13:30.99	1503.7 ± 29.2	180.7 ± 3.2	0.77 × 0.64	50.9	0.73 ± 0.02	0.61 ± 0.02	58.2 ± 6.1	3270 ± 140.0	2.9 - 2.7 ± 0.07
Per-emb-12-B	3:29:10.43	31:13:32.15	434.2 ± 7.9	128.6 ± 3.2	0.49 × 0.43	119.9	0.46 ± 0.02	0.33 ± 0.02	116.4 ± 9.8	-99.0 ± -99.0	3.7 - 3.3 ± 0.08
Per-emb-17-A	3:27:39.10	30:13:03.08	26.1 ± 0.5	22.9 ± 0.2	0.28 × 0.17	21.0	0.11 ± 0.01	0.062 ± 0.01	15.0 ± 8.8	55.0 ± 7.0	2.2 - 2.1 ± 0.07
Per-emb-17-B	3:27:39.11	30:13:02.85	20.4 ± 0.5	15.9 ± 0.2	0.31 × 0.2	18.6	0.16 ± 0.01	0.11 ± 0.01	7.1 ± 11.3	-99.0 ± -99.0	2.8 ± 0.09
Per-emb-18	3:29:11.26	31:18:31.03	145.2 ± 1.4	29.0 ± 0.3	0.74 × 0.31	72.3	0.70 ± 0.01	0.19 ± 0.01	75.4 ± 0.3	150.0 ± 9.0	3.0 - 2.8 ± 0.07
Per-emb-21	3:29:10.66	31:18:20.10	49.3 ± 0.5	44.3 ± 0.3	0.29 × 0.18	21.7	0.083 ± 0.01	0.065 ± 0.01	32.4 ± 17.8	53.0 ± 4.0	2.4 ± 0.08
Per-emb-22-A	3:25:22.40	30:45:13.21	33.6 ± 0.7	18.8 ± 0.2	0.36 × 0.23	35.9	0.27 ± 0.01	0.16 ± 0.01	49.7 ± 3.4	74.0 ± 12.0	2.6 - 2.2 ± 0.08
Per-emb-22-B	3:25:22.35	30:45:13.14	10.1 ± 0.2	8.5 ± 0.2	0.26 × 0.15	20.6	0.0 ± 0.0	0.0 ± 0.0	0.0 ± 0.0	-99.0 ± -99.0	2.7 - 2.2 ± 0.09
Per-emb-27-A	3:28:55.57	31:14:36.95	162.5 ± 2.1	108.5 ± 0.8	0.31 × 0.21	24.1	0.17 ± 0.01	0.14 ± 0.01	46.5 ± 10.0	290.0 ± 27.0	2.5 - 2.4 ± 0.07
Per-emb-27-B	3:28:55.56	31:14:36.38	26.8 ± 2.5	15.4 ± 0.8	0.40 × 0.22	25.4	0.29 ± 0.05	0.15 ± 0.02	29.0 ± 10.8	-99.0 ± -99.0	2.4 ± 0.09
Per-emb-2	3:32:17.92	30:49:47.85	571.8 ± 9.7	20.5 ± 0.7	1.22 × 0.83	173.8	1.20 ± 0.02	0.81 ± 0.01	172.6 ± 1.8	570.0 ± 34.0	2.9 ± 0.07
Per-emb-33-A	3:25:36.32	30:45:14.84	6.5 ± 0.8	22.4 ± 0.5	0.25 × 0.15	31.5	0.0 ± 0.0	0.0 ± 0.0	0.0 ± 0.0	740.0 ± 32.0	2.1 - 1.7 ± 0.1
Per-emb-33-B	3:25:36.31	30:45:15.09	31.9 ± 1.4	26.5 ± 0.5	0.39 × 0.21	11.9	0.28 ± 0.02	0.13 ± 0.01	5.7 ± 4.6	-99.0 ± -99.0	2.3 ± 0.08
Per-emb-33-C	3:25:36.38	30:45:14.64	163.0 ± 1.8	79.4 ± 0.5	0.39 × 0.28	21.2	0.27 ± 0.01	0.22 ± 0.01	23.0 ± 2.8	-99.0 ± -99.0	2.9 ± 0.08
L1448NW-A	3:25:35.67	30:45:34.08	49.8 ± 0.5	39.7 ± 0.2	0.31 × 0.19	23.1	0.16 ± 0.01	0.075 ± 0.01	33.6 ± 1.9	82.0 ± 7.0	2.5 - 2.3 ± 0.07
L1448NW-B	3:25:35.68	30:45:34.34	14.8 ± 0.2	19.2 ± 0.2	0.27 × 0.17	18.1	0.0 ± 0.0	0.037 ± 0.0	18.2 ± 0.0	-99.0 ± -99.0	1.9 ± 0.08
Per-emb-44-A	3:29:03.76	31:16:03.81	99.0 ± 1.1	80.5 ± 0.5	0.32 × 0.19	20.7	0.16 ± 0.01	0.093 ± 0.01	23.9 ± 2.3	400.0 ± 19.0	2.4 - 2.2 ± 0.07
Per-emb-44-B	3:29:03.74	31:16:03.80	158.1 ± 1.8	74.9 ± 0.5	0.42 × 0.26	27.3	0.32 ± 0.01	0.20 ± 0.01	33.6 ± 1.6	-99.0 ± -99.0	3.1 - 3.0 ± 0.08
SVS13B	3:29:03.07	31:15:51.72	222.2 ± 2.2	73.5 ± 0.5	0.43 × 0.35	53.0	0.36 ± 0.01	0.26 ± 0.01	75.2 ± 2.5	270.0 ± 28.0	2.7 ± 0.07
SVS13A2	3:29:03.38	31:16:01.62	13.9 ± 1.0	12.8 ± 0.5	0.29 × 0.17	18.1	0.11 ± 0.05	0.044 ± 0.03	10.5 ± 79.8	1.3 ± 4.3	2.2 - 2.0 ± 0.09
RAC1999 VLA20	3:29:04.25	31:16:09.14	4.4 ± 1.0	3.7 ± 0.5	0.28 × 0.19	13.7	0.11 ± 0.1	0.026 ± 0.1	136.5 ± 85.1	4.5 ± 3.0	1.7 ± 0.2
Per-emb-8	3:44:43.98	32:01:35.15	102.8 ± 2.7	64.4 ± 0.3	0.32 × 0.24	24.5	0.17 ± 0.01	0.14 ± 0.01	103.8 ± 4.7	120.0 ± 9.3	2.8 - 2.4 ± 0.07
Per-emb-8 Inner Disk	3:44:43.98	32:01:35.18	89.1 ± 0.7	64.4 ± 0.3	0.30 × 0.23	19.5	0.16 ± 0.01	0.094 ± 0.01	120.9 ± 2.6	120.0 ± 9.3	2.7 - 2.3 ± 0.07
Per-emb-8 Outer Disk	3:44:43.98	32:01:35.15	34.0 ± 2.2	64.4 ± 0.3	1.25 × 0.38	56.5	1.22 ± 0.09	0.32 ± 0.03	57.5 ± 1.6	-99.0 ± -99.0	...
Per-emb-35-A	3:28:37.09	31:13:30.74	22.6 ± 0.4	20.5 ± 0.2	0.29 × 0.17	21.6	0.085 ± 0.01	0.054 ± 0.01	36.4 ± 19.6	-99.0 ± -99.0	2.8 - 2.1 ± 0.08
Per-emb-35-B	3:28:37.22	31:13:31.70	16.8 ± 0.4	15.8 ± 0.2	0.28 × 0.16	22.3	0.078 ± 0.02	0.021 ± 0.02	40.3 ± 11.0	-99.0 ± -99.0	2.3 ± 0.08
Per-emb-36-A	3:28:57.37	31:14:15.79	129.2 ± 0.9	88.6 ± 0.4	0.29 × 0.23	22.8	0.16 ± 0.002	0.091 ± 0.01	105.7 ± 2.0	140. ± 5.0	2.4 - 2.3 ± 0.07
Per-emb-36-B	3:28:57.37	31:14:16.11	12.3 ± 0.7	29.6 ± 0.4	0.27 × 0.18	18.9	0.0 ± 0.01	0.0 ± 0.07	0.0 ± 0.0	-99.0 ± -99.0	2.0 ± 0.08
Per-emb-40-A	3:33:16.67	31:07:54.84	15.9 ± 0.3	14.1 ± 0.5	0.30 × 0.17	21.5	0.12 ± 0.01	0.04 ± 0.01	24.1 ± 3.6	17.0 ± 2.0	2.4 - 2.0 ± 0.08
Per-emb-40-B	3:33:16.69	31:07:55.20	0.9 ± 0.1	2.2 ± 0.5	0.28 × 0.16	20.8	0.0 ± 0.0	0.0 ± 0.0	0.0 ± 0.0	-99.0 ± -99.0	1.6 ± 0.15
Per-emb-48-A	3:27:38.28	30:13:58.60	4.0 ± 0.4	2.7 ± 0.1	0.36 × 0.22	21.4	0.23 ± 0.04	0.13 ± 0.02	23.5 ± 18.7	4.5 ± 2.0	2.0 ± 0.14
Per-emb-48-B	...	...	<0.4	<0.4 ± 0.1	0.36 × 0.22	21.4	0.23 ± 0.04	0.13 ± 0.02	23.5 ± 18.7	4.5 ± 2.0	<1.3
Per-emb-49-A	3:29:12.96	31:18:14.33	18.3 ± 0.4	15.5 ± 0.2	0.28 × 0.18	14.6	0.1 ± 0.01	0.052 ± 0.03	146.2 ± 12.3	20.0 ± 4.3	2.1 ± 0.08
Per-emb-49-B	3:29:12.98	31:18:14.44	4.9 ± 0.3	5.0 ± 0.2	0.26 × 0.16	20.8	0.0 ± 0.0	0.0 ± 0.0	0.0 ± 0.0	-99.0 ± -99.0	2.0 - 1.9 ± 0.1
Per-emb-55-A	3:44:43.29	32:01:31.19	3.3 ± 0.5	3.2 ± 0.3	0.29 × 0.18	25.3	0.078 ± 0.09	0.027 ± 0.06	79.2 ± 70.5	-99.0 ± -99.0	1.8 ± 0.11
Per-emb-55-B	3:44:43.33	32:01:31.65	0.5 ± 0.3	0.5 ± 0.3	0.29 × 0.17	22.6	0.052 ± 0.0	0.04 ± 0.0	17.5 ± 0.0	-99.0 ± -99.0	1.7 - 1.0 ± 0.32
L1448IRS1-A	3:25:09.45	30:46:21.92	73.4 ± 0.9	48.4 ± 0.4	0.33 × 0.2	23.4	0.21 ± 0.01	0.10 ± 0.01	29.3 ± 1.6	78.7 ± 14.0	2.5 - 2.3 ± 0.07
L1448IRS1-B	3:25:09.41	30:46:20.61	5.5 ± 0.7	5.5 ± 0.4	0.25 × 0.17	19.5	0.0 ± 0.0	0.0 ± 0.0	0.0 ± 0.0	-99.0 ± -99.0	2.2 ± 0.13
EDJ2009-269-A	3:30:44.02	30:32:46.82	11.1 ± 0.3	10.6 ± 0.2	0.26 × 0.17	18.5	0.043 ± 0.03	0.039 ± 0.01	147.3 ± 67.5	-99.0 ± -99.0	2.1 - 2.0 ± 0.1
EDJ2009-269-B	3:30:43.98	30:32:46.59	7.9 ± 0.3	7.5 ± 0.2	0.26 × 0.17	19.2	0.0 ± 0.07	0.0 ± 0.05	0.0 ± 0.0	-99.0 ± -99.0	1.9 ± 0.1
L1448IRS3A	3:25:36.50	30:45:21.84	101.0 ± 2.5	29.6 ± 0.5	0.75 × 0.39	136.5	0.73 ± 0.03	0.30 ± 0.02	134.1 ± 2.0	110.0 ± 9.0	2.7 - 2.4 ± 0.07
L1448IRS3A Inner Disk	3:25:36.50	30:45:21.78	165.4 ± 0.8	29.6 ± 0.5	0.26 × 0.16	20.0	0.0 ± 0.0	0.0 ± 0.0	0.0 ± 0.0	110.0 ± 9.0	3.0 - 2.6 ± 0.07
L1448IRS3A Outer Disk	3:25:36.50	30:45:21.84	84.4 ± 3.4	29.6 ± 0.5	0.75 × 0.39	136.5	0.73 ± 0.03	0.30 ± 0.02	134.1 ± 2.0	-99.0 ± -99.0	...

<sup>a</sup> The spectral index is calculated with respect to the 9.1 mm flux density given in Table 7 of Tychoniec et al. (2018b) under the assumption that  $F_\nu \propto \nu^\alpha$ . The range of spectral indices for most sources reflects the 9.1 mm flux density that is corrected and not corrected for free-free emission, respectively, in that study. The sources with only one spectral index listed could not be corrected for free-free emission. The formal uncertainty of the spectral index is quite low,  $\sim 0.1$ , even if 10% systematic uncertainty in the flux density is assumed due to the large difference in wavelength from 1.3 mm to 9.1 mm. We calculated the uncertainty in the spectral index following Chiang et al. (2012) Equation A5.

**Table 2.** Compact Masses vs. Extended Masses

Source	Gaussian mass ( $M_{\odot}$ )	Extended Mass ( $M_{\odot}$ )
Per-emb-2	$0.69 \pm 0.01$	$0.68 \pm 0.04$
Per-emb-12	$2.3 \pm 0.04$	$3.9 \pm 0.2$
Per-emb-12-A	$1.8 \pm 0.04$	...
Per-emb-12-B	$0.53 \pm 0.02$	...
Per-emb-17	$0.054 \pm 0.001$	$0.066 \pm 0.01$
Per-emb-17-A	$0.031 \pm 0.0005$	...
Per-emb-17-B	$0.024 \pm 0.0007$	...
Per-emb-18	$0.17 \pm 0.002$	$0.18 \pm 0.01$
Per-emb-21	$0.06 \pm 0.0005$	$0.063 \pm 0.005$
Per-emb-22	$0.053 \pm 0.001$	$0.088 \pm 0.014$
Per-emb-22-A	$0.041 \pm 0.0009$	...
Per-emb-22-B	$0.012 \pm 0.0002$	...
Per-emb-27	$0.24 \pm 0.003$	$0.35 \pm 0.03$
Per-emb-27-A	$0.204 \pm 0.0024$	...
Per-emb-27-B	$0.032 \pm 0.003$	...
Per-emb-33	$0.33 \pm 0.003$	$0.89 \pm 0.04$
Per-emb-33-A	$0.009 \pm 0.001$	...
Per-emb-33-B	$0.04 \pm 0.002$	...
Per-emb-33-C	$0.2 \pm 0.002$	...
L1448NW	$0.08 \pm 0.0009$	$0.1 \pm 0.009$
L1448NW-A	$0.060 \pm 0.0007$	...
L1448NW-B	$0.018 \pm 0.0003$	...
Per-emb-44	$0.31 \pm 0.002$	$0.48 \pm 0.02$
Per-emb-44-A	$0.12 \pm 0.001$	...
Per-emb-44-B	$0.19 \pm 0.002$	...
SVS13B	$0.27 \pm 0.003$	$0.33 \pm 0.03$
SVS13A2	$0.017 \pm 0.002$	$0.002 \pm 0.005$
RAC1999 VLA20	$0.005 \pm 0.001$	$0.003 \pm 0.002$
Per-emb-8	$0.15 \pm 0.003$	$0.15 \pm 0.01$
Per-emb-8 Inner Disk	$0.11 \pm 0.0009$	...
Per-emb-8 Outer Disk	$0.041 \pm 0.003$	...
Per-emb-35-A	$0.027 \pm 0.0005$	...
Per-emb-35-B	$0.020 \pm 0.0005$	...
Per-emb-36	$0.17 \pm 0.001$	$0.17 \pm 0.005$
Per-emb-36-A	$0.15 \pm 0.001$	...
Per-emb-36-B	$0.015 \pm 0.0009$	...
Per-emb-40-A	$0.019 \pm 0.0003$	...
Per-emb-40-B	$0.0017 \pm 0.0002$	...
Per-emb-48-A	$0.005 \pm 0.0005$	$0.005 \pm 0.002$
Per-emb-48-B	$<0.0005$	...
Per-emb-49-A	$0.022 \pm 0.0005$	...
Per-emb-49-B	$0.005 \pm 0.0003$	...
Per-emb-55-A	$0.003 \pm 0.0007$	...
Per-emb-55-B	$0.0007 \pm 0.0003$	...
L1448IRS1-A	$0.088 \pm 0.001$	...
L1448IRS1-B	$0.007 \pm 0.0009$	...
L1448IRS3A	$0.12 \pm 0.005$	$0.13 \pm 0.01$
L1448IRS3A Inner Disk	$0.02 \pm 0.001$	...
L1448IRS3A Outer Disk	$0.1 \pm 0.004$	...
EDJ2009-269-A	$0.014 \pm 0.0003$	...
EDJ2009-269-B	$0.01 \pm 0.0003$	...

Table 3. Line Integration Intervals and Resultant Noise

Source	$^{13}\text{CO}$ intervals	$^{13}\text{CO}$ rms	$\text{C}^{18}\text{O}$ intervals	$\text{C}^{18}\text{O}$ rms	SO intervals	SO rms	$\text{H}_2\text{CO}$ intervals	$\text{H}_2\text{CO}$ rms	$^{12}\text{CO}$ intervals	$^{12}\text{CO}$ rms
Per-emb-2	5.0-6.0, 8.0-9.5	3.33, 3.95	7.5-9.0, 5.0-6.25	2.16, 1.65	...	...	...	...	1.5-6.5, 9.0-15.0	5.8, 6.15
Per-emb-12	1.25-6.5, 6.5-9.75	5.59, 6.65	4.25-6.75, 7.75-9.0	3.34, 2.46	1.0-7.0, 8.0-11.75	6.24, 4.99	3.75-7.0, 8.0-11.0	3.64, 3.51	-1.5-6.5, 10.0-15.5	7.21, 6.05
Per-emb-17	0.5-4.5, 6.5-9.75	6.08, 5.52	3.0-4.75, 5.5-7.75	2.19, 2.19	-1.5-5.0, 5.25-10.25	6.6, 5.8	0.0-5.0, 5.25-9.75	4.54, 4.32	0.0-4.0, 7.5-14.0	6.56, 5.26
Per-emb-18	4.75-7.5, 9.25-11.5	4.79, 4.54	4.75-7.25, 8.75-11.5	3.22, 3.37	4.5-8.0, 8.25-11.5	4.83, 4.67	4.5-7.5, 9.25, 11.25	3.51, 3.08	3.0-5.0, 10.0 13.0	5.26, 4.41
Per-emb-21	...	...	...	...	...	...	...	...	...	...
Per-emb-22	2.25-3.75, 4.75-5.75	3.94, 3.33	2.75-4.0, 4.5-5.75	2.58, 2.58	1.75-5.75	5.21	3.0-4.0, 4.25-6.0	2.2, 2.79	-8.0-2.0, 7.5-16.0	8.1, 7.5
Per-emb-27	0.25-6.25, 9.5-10.5	7.03, 3.14	5.75-7.25, 7.5-9.0	2.58, 2.58	0.25-7.0, 7.25-11.0	7.0, 5.29	3.0-6.75, 7.75-10.0	3.91, 3.09	-28.5-6.0, 9.5-20.0	13.56, 13.58
Per-emb-33	1.25-4, 5.5-7.0	4.99, 3.20	1.25-4.0, 5.5-7.0	2.25, 1.65	1.25-4.5, 4.5-8.0	4.74, 4.91	2.75-4.0, 5.25-6.25	2.25, 2.05	-5.5-1.5, 4.5-8.0	6.88, 5.02
L1448NW	0.75-3.5, 5.25-7.75	4.95, 4.74	1.0-3.75, 4.0, 7.25	3.66, 3.39	2.25-5.0	4.41	1.5-6.25	4.12	-9.0-3.5, 6.0-16.0	8.4, 7.54
Per-emb-44	6.75-7.5, 9.0, 11.0	2.78, 4.17	6.0-8.5, 8.75, 10.0	3.63, 2.34	4.75-8.5, 8.75-11.75	6.36, 5.73	4.25-8.5, 8.75-11.75	3.63, 2.34	-25.0-0.0, 10.0-20.0	4.42, 4.22
Per-emb-8	5.75-8.75, 12.0-14.5	5.09, 4.68	6.0-9.25, 11.75-14.0	3.57, 3.02	7.5-10.0, 10.75-12.0	4.04, 2.99	6.75-10.25, 11.0-13.5	3.42, 2.93	4.5-8.5, 13.0-16.5	4.89, 4.61
Per-emb-55	...	...	...	...	...	...	...	...	4.5-8.5, 11.5-16.0	4.90, 5.16
Per-emb-35	5.75-6.25, 6.5-7.25	2.52, 2.91	5.25-8.0	4.31	5.5-7.25, 7.5-9.5	3.35, 3.55	5.5-7.5, 7.75-10.5	2.87, 3.63	2.0-7.5, 10.0-14.0	6.0, 5.2
Per-emb-36	3.5-5.75, 9.0-11.0	4.68, 4.17	4.5-6.5	3.14	4.5-7.0, 7.25-9.0	4.29, 3.65	4.0-6.25	2.87	-3.0-5.0, 9.5-16.0	7.81, 7.1
Per-emb-40	5.0-6.5	3.91, 4.18	5.0-7.75	3.38	...	...	...	...	-3.5-5.0, 8.5-13.5	8.03, 6.28
Per-emb-48	...	...	...	...	...	...	...	...	...	...
Per-emb-49	...	...	...	...	...	...	...	...	...	...
L1448RS1	...	...	...	...	...	...	...	...	...	...
L1448RS3A	2.5-3.75, 6.25-9.0	2.96, 4.19	2.25-3.75, 6.25-9.0	2.42, 3.18	3.0-4.25, 4.25-8.0	3.1, 5.07	3.0-3.75, 5.25-7.0	1.83, 2.6	-1.0-1.5, 6.5-11.0	4.35, 5.61
EDJ2009-269	...	...	...	...	...	...	...	...	5.5-8.0	5.04

Table 4. Molecules and Rotation Characteristics

Source	Class	Separation ( $''$ , AU)	Outflow PA <sup>a</sup> ( $^{\circ}$ )	Gradient PA <sup>b</sup> ( $^{\circ}$ )	<sup>12</sup> CO	<sup>13</sup> CO	C <sup>18</sup> O	H <sub>2</sub> CO	SO	Rotation vs. Outflow	Disk Frag. Possible?
Per-emb-2	0	0.080, 24.0	128	232 (104)	Outflow	Rotation	Rotation	...	...	Perpendicular	Yes
Per-emb-12	0	1.830, 548.9	175, 205	...	Outflow	Indistinct	Indistinct	...	Indistinct	Indistinct	No
Per-emb-17	0	0.278, 83.3	240	180/133 (60/107)	Outflow	Rotation	Rotation	Outflow+Rotation	Outflow+Rotation	Perpendicular	Yes
Per-emb-18	0	0.085, 25.6	169	78 (91)	Outflow	Rotation	Rotation	Rotation	Rotation	Perpendicular	Yes
Per-emb-22	0	0.751, 225.4	306	246 (60)	Outflow	Rotation	Rotation	Indistinct	Indistinct	Perpendicular	Yes
Per-emb-27	0	0.620, 186.0	204, 285	...	Outflow	Indistinct	Indistinct	Outflow/Indistinct	Outflow	Indistinct	No
Per-emb-33	0	0.264, 79.2	301, 284	212 (89)	Outflow	Rotation	Rotation	Rotation	Outflow?	Perpendicular	Yes
	0	0.795, 238.4									
L1448NW	0	0.251, 75.3	305	224 (81)	Outflow	Rotation	Rotation	Indistinct	Indistinct	Perpendicular	Yes
Per-emb-44	0/I	0.300, 90.0	147	220 (73)	Outflow	Rotation	Rotation	Rotation?	Rotation?	Perpendicular	Yes
Per-emb-35	I	1.908, 572.3	292, 279	Outflow	Outflow?	Indistinct	Indistinct	Indistinct	Indistinct	No?	No?
Per-emb-36	I	0.311, 93.4	24	...	Outflow	Indistinct	Indistinct	Rotation?	Outflow?	Indistinct	No?
Per-emb-40	I	0.391, 117.4	123?	...	Outflow/Rotation	Indistinct	Indistinct	...	...	...	...
Per-emb-48	I	0.346, 103.7	...	...	Indistinct	...	...	...	...	...	...
Per-emb-49	I	0.313, 93.8	...	...	...	...	...	...	...	...	...
Per-emb-55	I	0.618, 185.3	121?	...	Outflow	...	...	...	...	...	...
L1448IRS1	I	1.424, 427.0	113	212 (99)	Rotation	...	...	...	...	Perpendicular	Yes?
EDJ2009-269	II	0.524, 157.3	...	...	Indistinct	...	...	...	...	...	...
Per-emb-35-A	I		292	201 (91)	Outflow	Indistinct	Indistinct	Rotation?	Indistinct	Perpendicular?	...
Per-emb-35-B	I		279	233 (46)	Outflow	Outflow?	Rotation?	Rotation?	Indistinct	Perpendicular?	...
L1448IRS3A	I		38	313 (85)	Outflow?	Rotation	Rotation	Rotation	Rotation	Perpendicular	...
Per-emb-8	0		314	44 (90)	Outflow/Rotation	Rotation	Rotation	Rotation	Rotation	Perpendicular	...
Per-emb-21	0		80?	...	Outflow	...	...	...	...	...	...
SYS13B	0		160	...	Outflow	...	...	...	...	...	...

NOTE.—This table examines what kinematics are being displayed by each molecular line. The ellipsis symbols (...) correspond to non-detections. The question marks (?) following a descriptor indicate that the line might display a certain kinematic signature, but that ambiguity remains. We expect that the outflow position angle (PA) and gradient PA to have a typical uncertainty of  $10^{\circ}$ .

<sup>a</sup> This is measured from the <sup>12</sup>CO data presented in this paper except for Per-emb-36 and L1448 IRS1. To measure the outflow PA, we draw a line that best bisects the outflow cavity. We adopt the outflow PA value from Plunkett et al. (2013) for Per-emb-36 because of how wide the outflow is. For L1448 IRS1, <sup>12</sup>CO is tracing rotation, thus we use the scattered light nebula in the image from Foster & Goodman (2006).

<sup>b</sup> The PA of the velocity gradient is measured by drawing a line from the peaks of the blue- and red-shifted integrated intensity maps, generally C<sup>18</sup>O.

**Table 5.** Class 0 Multiple Systems

Source	Separation (")	Separation (AU)	Flux Difference (Log [F <sub>1</sub> /F <sub>2</sub> ])	Type
Per-emb-2	0.080 ± 0.006	24.0 ± 1.7	0.17 ± 0.15	Class 0
Per-emb-18	0.085 ± 0.004	25.6 ± 1.2	-0.02 ± 0.12	Class 0
Per-emb-5	0.097 ± 0.006	29.1 ± 1.8	0.26 ± 0.07	Class 0
L1448NW	0.251 ± 0.004	75.3 ± 1.7	0.17 ± 0.03	Class 0
Per-emb-33	0.264 ± 0.008	79.2 ± 2.3	0.12 ± 0.05	Class 0
Per-emb-17	0.278 ± 0.014	83.3 ± 4.0	0.75 ± 0.08	Class 0
Per-emb-44	0.300 ± 0.003	90.0 ± 0.9	0.48 ± 0.02	Class 0
Per-emb-27	0.620 ± 0.003	186.0 ± 0.9	0.75 ± 0.03	Class 0
Per-emb-22	0.751 ± 0.004	225.4 ± 1.3	0.51 ± 0.05	Class 0
Per-emb-33	0.795 ± 0.004	238.4 ± 1.3	0.33 ± 0.04	Class 0
Per-emb-12	1.830 ± 0.002	548.9 ± 0.5	1.04 ± 0.02	Class 0
Per-emb-11	2.951 ± 0.008	885.4 ± 2.2	0.93 ± 0.08	Class 0
Per-emb-44+SVS13A2	5.314 ± 0.004	1594.2 ± 1.2	1.78 ± 0.03	Class 0/I
Per-emb-32	6.066 ± 0.022	1820.0 ± 6.5	-0.16 ± 0.27	Class 0/I
Per-emb-33+L1448IRS3A	7.317 ± 0.004	2195.2 ± 1.2	-0.24 ± 0.02	Class 0-Class I
Per-emb-26+Per-emb-42	8.104 ± 0.005	2431.3 ± 1.6	1.97 ± 0.03	Class 0-Class I
Per-emb-11	9.469 ± 0.025	2840.6 ± 7.6	0.76 ± 0.13	Class 0
Per-emb-8+Per-emb-55	9.557 ± 0.013	2867.2 ± 3.8	2.38 ± 0.10	Class 0-Class I
Per-emb-37+EDJ2009+235	10.556 ± 0.009	3166.7 ± 2.9	1.53 ± 0.11	Class 0-Class II
Per-emb-13+IRAS4B'	10.654 ± 0.005	3196.2 ± 1.6	0.81 ± 0.02	Class 0-Class 0
Per-emb-21+Per-emb-18	13.252 ± 0.004	3975.7 ± 1.3	-0.44 ± 0.02	Class 0-Class 0
B1-bS+Per-emb-41	13.957 ± 0.014	4187.1 ± 4.2	2.08 ± 0.09	Class 0-Class 0/I
Per-emb-44+SVS13B	14.932 ± 0.002	4479.7 ± 0.7	0.40 ± 0.01	Class 0/I-Class 0
Per-emb-16+Per-emb-28	16.063 ± 0.037	4818.9 ± 11.1	-0.05 ± 0.17	Class 0-Class 0
B1-bN+B1-bS	17.395 ± 0.009	5218.4 ± 2.6	0.31 ± 0.03	Class 0-Class 0
Per-emb-33+L1448NW	21.503 ± 0.004	6450.8 ± 1.3	-0.23 ± 0.02	Class 0-Class 0
Per-emb-18+Per-emb-49	27.474 ± 0.007	8242.3 ± 2.0	0.33 ± 0.03	Class 0-Class I
Per-emb-12+Per-emb-13	29.739 ± 0.002	8921.7 ± 0.7	1.04 ± 0.01	Class 0-Class 0
Per-emb-36+Per-emb-27	31.420 ± 0.001	9426.0 ± 0.4	0.15 ± 0.01	Class 0-Class I
Per-emb-6+Per-emb-10	31.947 ± 0.005	9584.2 ± 1.6	-0.28 ± 0.03	Class 0-Class 0
Per-emb-37+EDJ2009+233	33.704 ± 0.006	10111.3 ± 1.7	-0.62 ± 0.04	Class 0-Class II
Per-emb-44+SVS13C	34.528 ± 0.001	10358.5 ± 0.4	-0.21 ± 0.01	Class 0/I-Class 0
Per-emb-32+EDJ2009+366	36.605 ± 0.010	10981.6 ± 3.1	-1.31 ± 0.11	Class 0/I-Class II

NOTE—This table includes Class 0 + Class 0, Class 0 + Class I, and Class 0 + Class II multiple systems. The flux difference is calculated in the 9 mm band. The distance has been revised to 300 pc for the physical separation distance.

**Table 6.** Class I Multiple Systems

Source	Separation ( $''$ )	Separation (AU)	Flux Difference (Log $[F_1/F_2]$ )
Per-emb-36	$0.311 \pm 0.005$	$93.4 \pm 1.6$	$0.80 \pm 0.02$
Per-emb-49	$0.313 \pm 0.009$	$93.8 \pm 2.6$	$0.46 \pm 0.11$
Per-emb-48	$0.346 \pm 0.019$	$103.7 \pm 5.7$	$0.06 \pm 0.17$
Per-emb-40	$0.391 \pm 0.022$	$117.4 \pm 6.7$	$0.94 \pm 0.19$
Per-emb-55	$0.618 \pm 0.009$	$185.3 \pm 2.6$	$0.14 \pm 0.07$
EDJ2009-183	$1.025 \pm 0.028$	$307.6 \pm 8.3$	$0.45 \pm 0.13$
L1448IRS1	$1.424 \pm 0.015$	$427.0 \pm 4.6$	$1.02 \pm 0.09$
Per-emb-35	$1.908 \pm 0.003$	$572.3 \pm 0.9$	$0.23 \pm 0.04$
EDJ2009-156	$3.107 \pm 0.011$	$932.1 \pm 3.3$	$0.17 \pm 0.13$
Per-emb-58+Per-emb-65	$28.878 \pm 0.023$	$8663.3 \pm 6.9$	$-0.44 \pm 0.13$

NOTE—This table includes only Class I + Class I multiple systems. The flux difference is calculated in the 9 mm band. The distance has been revised to 300 pc for the physical separation distance.

**Table 7.** Class II Multiple Systems

Source	Separation ( $''$ )	Separation (AU)	Flux Difference (Log $[F_1/F_2]$ )
EDJ2009-269	$0.524 \pm 0.007$	$157.3 \pm 2.1$	$0.12 \pm 0.08$
EDJ2009-156	$3.107 \pm 0.011$	$932.1 \pm 3.3$	$0.17 \pm 0.13$

NOTE—This table includes only Class II + Class II multiple systems. The flux difference is calculated in the 9 mm band. The distance has been revised to 300 pc for the physical separation distance.